

Cosmic magnification in beyond-Horndeski gravity

Didam G.A. Duniya^{1,*} and Bishop Mongwane^{2,†}

¹*Department of Physics & Astronomy, Botswana International University of Science and Technology, Palapye, Botswana*

²*Department of Mathematics & Applied Mathematics, University of Cape Town, South Africa*

(Dated: July 9, 2024)

The cosmic magnification is able to probe the geometry of large scale structure on cosmological scales, thereby providing another window for probing theories of the late-time accelerated expansion of the Universe. It holds the potential to reveal new information on the nature of dark energy and modified gravity. By using the angular power spectrum, with all known relativistic corrections incorporated, we investigated cosmic magnification in beyond-Horndeski gravity. We probed both the total relativistic signal, and the individual relativistic signals. Our results suggest that surveys at low redshifts ($z \lesssim 0.5$) will be able to measure directly the total relativistic signal in the total magnification angular power spectrum without the need for multi-tracer analysis (to beat down cosmic variance). Similarly, for the Doppler signal, our results indicate that it can also be measured directly at the given low redshifts. However, for the integrated-Sachs-Wolfe, the time-delay, and the (gravitational) potential signals, respectively, it will require going to high redshifts ($z \gtrsim 3$) for the signals to surpass cosmic variance. For actual detectability though, proper quantitative methods and error analysis (not considered in this work) will need to be taken into account, i.e. in addition to cosmic variance. We also found that the beyond-Horndeski gravity boosts relativistic effects; consequently, cosmic magnification. Conversely, relativistic effects enhance the potential of the total magnification angular power spectrum to detect the imprint of beyond-Horndeski gravity.

Keywords: Alternative gravity theories; Dark energy; Gravitation; Relativistic aspects of cosmology

I. INTRODUCTION

The beyond-Horndeski gravity [1–9] is one of the most extensive modified gravity (MG) models [10, 11] currently in cosmology. Its description of gravity provides a means for a generalized approach of confronting theoretical ideas (of the late-time cosmic accelerated expansion) with current and future observational survey data. The model appears to combine, in a single description, a broad spectrum of well-known existing theories, including dark energy (DE) models [12–17], the scalar-tensor gravity models and their Horndeski extensions, the $f(R)$ gravity and the Horava-Lifshitz gravity models [10–12]. This theory provides a unified framework for cosmological perturbations about the well-known Friedmann-Robertson-Walker universe, at linear order. Moreover, rather than probing individual models, the cosmological observables of the beyond-Horndeski gravity are instead probed; from where the implication for various models may be inferred. Thus, in view of upcoming precise, large-volume surveys and, given its extensive theoretical reach, it is vital to probe its imprint in the cosmic magnification [13, 18–27].

Cosmic magnification is one of the important observables in modern cosmology. It will be crucial in interpreting measurements of cosmological distances; thus, providing a good means of probing the geometry of large scale structure. The weak (gravitational) lensing [18–21] is known as the standard source of cosmic magnification. However, cosmic magnification is only one of the

effects (along with cosmic shear, see e.g. [19–21, 28–30]) of weak lensing. Moreover, weak lensing is not the only source of cosmic magnification, others include [27]: (1) Doppler effect, which is sourced by the line-of-sight relative velocity between the source and the observer, (2) integrated-Sachs-Wolfe (ISW) effect, which is sourced by the integral of the time-rate of change of the gravitational potentials, (3) (cosmological) time delay, which is an integrated effect of the gravitational potentials, and (4) source-observer (gravitational) potential-well effect. The cosmic magnification manifests in large scale structure in various forms, e.g. a source moving towards an observer will appear to experience a boost in flux—this is Doppler magnification [23–25]. Cosmic magnification owing to time-delay effects manifests by broadening of the observed flux. The potential well between the source and the observer can also cause magnification if it is deep enough; particularly, when the observer is at the bottom of the potential well and the source is at the top, e.g. signals from sources with sufficiently lower masses relative to our galaxy (the Milky Way) will appear magnified upon reaching the earth (assuming they are close enough, and other effects are negligible). These last four effects are commonly referred to as “relativistic effects” (see e.g. [2, 13–16, 22–25, 31, 32]).

By probing the geometry of large scale structure, the cosmic magnification possesses the potential to provide new information on the nature of DE and MG, on the given scales (and redshifts). Moreover, upcoming surveys of large scale structure, which are able to put the cosmic magnification to the test, will extend to very large cosmic scales up to near and beyond the Hubble horizon; reaching high redshifts: on these cosmological scales and redshifts, most relativistic effects become significant. Hence,

* duniyaa@biust.ac.bw

† bishop.mongwane@uct.ac.za

relativistic effects will be key to revealing the strength of the cosmic magnification as a cosmological probe, and to understanding the nature of MG (and DE). Thus, in order to realise the full potential of the cosmic magnification, we need to correct for the relativistic effects in the observed overdensity of magnified sources (“magnification overdensity,” henceforth).

In this paper, we study the cosmic magnification in the beyond-Horndeski gravity, by probing the angular power spectrum of the observed, relativistic magnification overdensity, on large scales. The goal is to analyse the large-scale imprint of beyond-Horndeski gravity, and the relativistic effects, in the magnification angular power spectrum. The structure of the paper is as follows. In §II we discuss the Universe with beyond-Horndeski gravity. In §III we outline the observed (relativistic) magnification overdensity, and in §IV, we analyse the associated angular power spectrum. We conclude in §VI.

II. BEYOND-HORNDESKI GRAVITY

In this work, we consider the beyond-Horndeski gravity in the form of a Unified Dark Energy (UDE) [1–3]. Henceforth, we assume a late-time universe dominated by matter (dark plus baryonic) and UDE only.

A. The background cosmological equations

Given the background energy density $\bar{\rho}_A$ and the background pressure \bar{p}_A of matter ($A=m$) and of UDE ($A=x$), the Friedmann equation is given by

$$\begin{aligned} \mathcal{H}^2 &= \frac{8\pi G_{\text{eff}} a^2}{3} (\bar{\rho}_m + \bar{\rho}_x), \\ &= \mathcal{H}^2 (\Omega_m + \Omega_x), \end{aligned} \quad (1)$$

where $8\pi G_{\text{eff}} \equiv 1/M^2$, with M being an effective mass; $\mathcal{H} = a'/a$ is the comoving Hubble parameter, $a = a(\eta)$ is the cosmic scale factor, a prime denotes derivative with respect to conformal time η and, Ω_m and Ω_x are the matter and the UDE density parameters, respectively.

The associated background acceleration equation, is

$$2\mathcal{H}' + \mathcal{H}^2 = -8\pi G_{\text{eff}} a^2 (\bar{p}_m + \bar{p}_x). \quad (2)$$

The conservation of the total energy-momentum tensor leads to the matter and the UDE background energy density evolution equations, given by

$$\begin{aligned} \bar{\rho}'_m + 3\mathcal{H}(1 + w_m)\bar{\rho}_m &= 0, \\ \bar{\rho}'_x + 3\mathcal{H}(1 + w_x)\bar{\rho}_x &= \alpha_M \mathcal{H} \frac{\bar{\rho}_x}{\Omega_x}, \end{aligned} \quad (3)$$

where $w_A = \bar{p}_A/\bar{\rho}_A$ are the equation of state parameters, and we have

$$\alpha_M \equiv \frac{2M'}{\mathcal{H}M} = -\frac{G'_{\text{eff}}}{\mathcal{H}G_{\text{eff}}},$$

being the mass-evolution parameter, which governs the rate of evolution of M ; with G_{eff} being as given by (1).

Consequently, the evolution of the UDE equation of state parameter, is given by

$$\begin{aligned} w'_x &= -3\mathcal{H} \left(1 + w_x - \frac{\alpha_M}{3\Omega_x} \right) (c_{ax}^2 - w_x), \\ &= -3\mathcal{H} (1 + w_{x,\text{eff}}) (c_{ax}^2 - w_x), \end{aligned} \quad (4)$$

where $w_{x,\text{eff}}$ denotes an “effective” equation of state parameter for UDE, and $c_{ax}^2 = \bar{p}'_x/\bar{\rho}'_x$ is the square of the adiabatic sound speed of UDE.

B. The perturbed cosmological equations

Here we outline the perturbed field and conservation equations in a universe with UDE. We adopt a flat space-time metric, given by

$$ds^2 = a(\eta)^2 [-(1 + 2\Phi)d\eta^2 + (1 - 2\Psi)d\vec{x}^2], \quad (5)$$

where Φ and Ψ are the (gauge-invariant) temporal and spatial metric potentials, respectively [1, 2] (see also Appendix A).

The spatial metric potential evolves according to the equation given by

$$\Psi' + \mathcal{H}\Phi = -4\pi G_{\text{eff}} a^2 \sum_A (\bar{\rho}_A + \bar{p}_A) V_A, \quad (6)$$

where V_A are the (gauge-invariant) velocity potentials, with the UDE velocity potential being given by

$$8\pi G_{\text{eff}} (\bar{\rho}_x + \bar{p}_x) [V_x + \Pi] \equiv -2\alpha_B \mathcal{H} a^{-2} (\Pi' + \mathcal{H}\Pi - \Phi), \quad (7)$$

where Π is a scalar degree of freedom of the Lagrangian (with dimension of per mass). (This should not be confused with anisotropic stress potentials, as widely used in standard-DE literature.) The metric potentials are related by

$$\Psi - \Phi = 8\pi G_{\text{eff}} a^2 \sum_A \sigma_A, \quad (8)$$

where σ_A are the effective comoving anisotropic stress potentials (having dimension of M^2), and σ_x is given by

$$\begin{aligned} 8\pi G_{\text{eff}} \sigma_x &\equiv a^{-2} \left[\alpha_M \mathcal{H}\Pi - \alpha_T (\Psi + \mathcal{H}\Pi) \right. \\ &\quad \left. - \alpha_H (\Pi' + \mathcal{H}\Pi - \Phi) \right], \end{aligned} \quad (9)$$

where α_H is the Horndeski parameter, which measures deviation from Horndeski gravity. The temporal metric potential evolves according to [2]

$$\Phi' + (1 + \lambda_1)\mathcal{H}\Phi = \lambda_2 \mathcal{H}\Psi + \lambda_3 \mathcal{H}^2 \Pi - 4\pi G_{\text{eff}} a^2 \lambda_4 \bar{\rho}_m V_m, \quad (10)$$

where henceforth, we assume matter has zero pressure (i.e. $\bar{p}_m = 0$, and all pressure-related parameters vanish), and we have

$$\begin{aligned}\lambda_1 &\equiv \alpha_T + \alpha_H(\gamma_5 - \gamma_4) + \alpha_B(1 + \alpha_T - \alpha_H\gamma_4) \\ &\quad - \frac{\alpha'_H}{\mathcal{H}\alpha_H} - \beta_1\left(\frac{1 + \alpha_H}{\alpha_H}\right), \\ \lambda_2 &\equiv \frac{\alpha'_T}{\mathcal{H}} - (1 + \alpha_T)\frac{\alpha'_H}{\mathcal{H}\alpha_H} - \alpha_H\gamma_6 - \beta_1\left(\frac{1 + \alpha_T}{\alpha_H}\right), \\ \lambda_3 &\equiv \beta_2 + \beta_1\left(\frac{\alpha_M - \alpha_T}{\alpha_H} - 1\right), \quad \lambda_4 \equiv 1 + \alpha_T - \alpha_H\gamma_4,\end{aligned}$$

where α_T is the tensor speed parameter, which measures the difference between the gravitational waves speed c_T and the speed of light $c = 1$, with $c_T^2 = 1 + \alpha_T$ and, α_B is the kinetic braiding [1–7], which measures the kinetic mixing between gravitational and scalar degrees of freedom in the Lagrangian; with

$$\begin{aligned}\beta_1 &\equiv \alpha_T + \alpha_B\lambda_4 - \alpha_M - \alpha_H\gamma_1, \\ \beta_2 &\equiv (\alpha_M - \alpha_T)\frac{\alpha'_H}{\alpha_H\mathcal{H}} + (\alpha_H - \alpha_M + \alpha_H\gamma_4 - 1)\frac{\mathcal{H}'}{\mathcal{H}^2} \\ &\quad + \frac{\alpha'_T - \alpha'_M}{\mathcal{H}} - \alpha_H\gamma_3 + \lambda_4\left[1 + \alpha_B - \frac{4\pi G_{\text{eff}}a^2}{\mathcal{H}^2}\bar{\rho}_m\right].\end{aligned}$$

where $\gamma_1, \gamma_3, \gamma_4, \gamma_5$ and γ_6 are dimensionless parameters (see Appendix A). The scalar Π , given in (7), evolves by

$$\Pi' + \left(1 + \frac{\alpha_T - \alpha_M}{\alpha_H}\right)\mathcal{H}\Pi = \left(\frac{1 + \alpha_H}{\alpha_H}\right)\Phi - \left(\frac{1 + \alpha_T}{\alpha_H}\right)\Psi. \quad (11)$$

The conservation of the energy-momentum tensor (see Appendix B) leads to the evolution equation for the matter velocity potential V_m and (gauge-invariant) comoving overdensity Δ_m , respectively, given by

$$V'_m + \mathcal{H}V_m = -\Phi, \quad (12)$$

$$\Delta'_m - \frac{9}{2}\mathcal{H}^2\Omega_x(1 + w_x)[V_m - V_x] = -\nabla^2V_m, \quad (13)$$

where henceforth, we adopt the comoving overdensity Δ_A , which avoids large-scale unphysical anomalies (e.g. [31, 33]), given by

$$\bar{\rho}_A\Delta_A \equiv \delta\rho_A + \bar{\rho}'_AV_A, \quad (14)$$

with $\delta\rho_A$ being the energy density perturbations (see Appendix A for the expression of $\delta\rho_x$, and $\delta\rho_m$ is prescribed by the energy-momentum tensor in Appendix B).

Similarly, the UDE comoving velocity potential evolves according to the equation:

$$V'_x + \mathcal{H}V_x = -\Phi - \frac{c_{sx}^2}{1 + w_x}\frac{\Delta_x}{\mathcal{H}} - \frac{2\nabla^2\sigma_x}{3(1 + w_x)\bar{\rho}_x} - \alpha_M\mathcal{H}\mathcal{A}, \quad (15)$$

where $\Omega_x(1 + w_x)\mathcal{A} \equiv V_x - \sum_A\Omega_A(1 + w_A)V_A$, and c_{sx} is the UDE physical sound speed, given by

$$\begin{aligned}c_{sx}^2 &= -2\frac{(1 + \alpha_B)^2}{\alpha_K + 6\alpha_B^2}\left\{1 + \alpha_T - \frac{1 + \alpha_H}{1 + \alpha_B}\left(2 + \alpha_M - \frac{\mathcal{H}'}{\mathcal{H}^2}\right)\right. \\ &\quad \left. - \frac{1}{\mathcal{H}}\left(\frac{1 + \alpha_H}{1 + \alpha_B}\right)'\right\} - 3\frac{(1 + \alpha_H)^2}{\alpha_K + 6\alpha_B^2}\Omega_m,\end{aligned}$$

with α_K being the kineticity, which measures the kinetic energy contribution of the scalar field, and $\alpha_K + 6\alpha_B^2 > 0$.

Although Horndeski gravity ($\alpha_H = 0$), like general relativity, only supports gravitational waves that propagate with luminal speed, beyond-Horndeski gravity ($\alpha_H \neq 0$) is able to support gravitational waves that travel at super-luminal speed ($c_T > 1$) or sub-luminal speed ($c_T < 1$). Noting that a recent source detection in gravitational and electromagnetic radiation suggested that $\alpha_T = 0$, it is still possible that α_T varies for higher redshift and possibly with frequency (e.g. [34, 35]). Generally, in a Lorentz-invariant system, gravitational waves will propagate at the speed of light [34], and this implicitly ensures that the speed of the gravitational waves is independent of scale, time and energy [35]. Thus, to admit non-luminal sound speeds, the gravity action (or Lagrangian) will need to be modified to allow time dependence of the cosmological background solution of the scalar degree of freedom—such time dependence will spontaneously break Lorentz invariance and provide a non-trivial medium for gravitational waves to travel through [34]. Moreover, a modification which admits a time-dependent, effective mass instead of the constant Planck mass will also spontaneously break Lorentz invariance, by inducing energy variation (and dependence) in the gravitational wave sector. These types of modifications that carry time dependence are already enshrined in the beyond-Horndeski gravity. In fact, the time dependence of the effective mass in the beyond-Horndeski gravity results in the breaking of the conservation of total energy and momentum, as shown in (3), (15) and (16). Therefore, the beyond-Horndeski gravity will naturally have $\alpha_T \neq 0$ (since α_H is non-zero); hence, a non-constant gravitational waves speed. And if the gravitational waves speed evolves, then it can be non-luminal. It should be pointed out that reverting from beyond-Horndeski to Horndeski gravity is non-trivial: it does not follow by merely setting $\alpha_H = 0$. As can be seen in e.g. (10) and (11), setting $\alpha_H = 0$ will lead to numerically unsolvable equations. In order to recover Horndeski gravity, one will need to return to first principles (from the Lagrangian). Hence, we restricted our analysis to remain completely within the beyond-Horndeski gravity.

In general, α_T , α_B and α_H are related, given by [2]

$$\alpha_T = \frac{4\alpha_H^2 + (\alpha_H - \alpha_B)\Upsilon_1}{(1 + \alpha_B)\Upsilon_1}, \quad \alpha_B = \alpha_H\left(1 - 5\frac{\Upsilon_2}{\Upsilon_1}\right),$$

where Υ_1 is the parameter that governs the deviation from Newton's law in astrophysical systems, and Υ_2 is the parameter that governs light bending around non-relativistic objects (both parameters are dimensionless constants); with $\Upsilon_1 = -0.11_{-0.67}^{+0.93}$ and $\Upsilon_2 = -0.22_{-1.19}^{+1.22}$ [4] (see also [8, 9]). We notice that $c_T^2 = 1 + \alpha_T = 1$ when $\alpha_H = 0$ (Horndeski gravity). Thus, enforcing $\alpha_T = 0$ will imply $\alpha_H = 0$, which will now mean pure Horndeski gravity (opposed to the subject of interest of this work). Moreover, doing so will greatly reduce the parameter space of the beyond-Horndeski gravity [35], and may limit

the chance of identifying the true imprint of the beyond-Horndeski gravity. Therefore, for generality, we do not restrict α_T to be zero.

The UDE comoving overdensity evolves according to

$$\begin{aligned} \Delta'_x - 3w_x \mathcal{H} \Delta_x &= \frac{9}{2} \mathcal{H}^2 (1 + w_x) \sum_A \Omega_A (1 + w_A) [V_x - V_A] \\ &\quad - (1 + w_x) \nabla^2 V_x + \frac{2\mathcal{H}}{\bar{\rho}_x} \nabla^2 \sigma_x + \alpha_M \mathcal{H} \mathcal{B}, \end{aligned} \quad (16)$$

where,

$$\begin{aligned} \Omega_x \mathcal{B} &\equiv V'_x - \Delta_x + \left[\frac{\alpha'_M}{\alpha_M} - \frac{1}{2} (1 + 9w - 2\alpha_M) \mathcal{H} \right] V_x \\ &\quad + \sum_A \Omega_A \left[\Delta_A - \frac{\bar{\rho}'_A}{\bar{\rho}_A} V_A - 3\mathcal{H} (1 + w_A) V_A \right]. \end{aligned}$$

Notice that (3), (15) and (16) tend to suggest that the given UDE corresponds to an interacting DE scenario in which the total energy-momentum tensor (see Appendix B) is not conserved: α_M breaks the energy-momentum conservation, in the sense that there are extra α_M terms in the UDE conservation equations that do not have counterparts in the matter conservation equations (even with $p_m \neq 0$).

Equations (2)–(4), (6), (10)–(13), (15), and (16) form the complete system of cosmological evolution equations.

III. THE OBSERVED MAGNIFICATION OVERDENSITY

The observed magnification overdensity [13, 19, 22, 26, 27], measured along the direction $-\mathbf{n}$ at a redshift z , is given here by

$$\Delta_{\mathcal{M}}^{\text{obs}}(\mathbf{n}, z) = \Delta_{\mathcal{M}}^{\text{std}}(\mathbf{n}, z) + \Delta_{\mathcal{M}}^{\text{rels}}(\mathbf{n}, z), \quad (17)$$

where we take the weak-lensing magnification as the “standard” term, given by

$$\Delta_{\mathcal{M}}^{\text{std}} \equiv -\mathcal{Q} \int_0^{r_S} dr (r - r_S) \frac{r}{r_S} \nabla_{\perp}^2 (\Phi + \Psi), \quad (18)$$

with $r_S = r(z_S)$ being the radial comoving distance at the source redshift z_S and, $\mathcal{Q} = \mathcal{Q}(z)$ being the magnification bias [36–40], and the relativistic corrections are given by

$$\Delta_{\mathcal{M}}^{\text{rels}} = \Delta_{\mathcal{M}}^{\text{Doppler}} + \Delta_{\mathcal{M}}^{\text{ISW}} + \Delta_{\mathcal{M}}^{\text{timedelay}} + \Delta_{\mathcal{M}}^{\text{potentials}}, \quad (19)$$

where,

$$\Delta_{\mathcal{M}}^{\text{Doppler}} \equiv -2\mathcal{Q} \left(1 - \frac{1}{r_S \mathcal{H}} \right) (\mathbf{n} \cdot \mathbf{V}), \quad (20)$$

$$\Delta_{\mathcal{M}}^{\text{ISW}} \equiv 2\mathcal{Q} \left(\frac{1}{r_S \mathcal{H}} - 1 \right) \int_0^{r_S} dr (\Phi' + \Psi'), \quad (21)$$

$$\Delta_{\mathcal{M}}^{\text{timedelay}} \equiv -\frac{2\mathcal{Q}}{r_S} \int_0^{r_S} dr (\Phi + \Psi), \quad (22)$$

$$\Delta_{\mathcal{M}}^{\text{potentials}} \equiv 2\mathcal{Q} \left\{ \Psi + \left(1 - \frac{1}{r_S \mathcal{H}} \right) \Phi \right\}, \quad (23)$$

where $-\mathbf{n} \cdot \mathbf{V} = -\partial V / \partial r \equiv V_{\parallel}$ is the line-of-sight component of the peculiar velocity, with V being the (gauge-invariant) velocity potential.

IV. THE MAGNIFICATION ANGULAR POWER SPECTRUM

The total (observed) magnification angular power spectrum observed at z_S , is given by

$$C_{\ell}(z_S) = \frac{4}{\pi^2} \left(\frac{43}{50} \right)^2 \int_0^{r_S} dk k^2 T(k)^2 P_{\Phi_p}(k) \left| F_{\ell}(k, z_S) \right|^2, \quad (24)$$

where P_{Φ_p} is the primordial power spectrum, $T(k)$ is the linear transfer function (see e.g. [41] for a fitting formula), k is the wavenumber, and we have

$$\begin{aligned} F_{\ell} &= \frac{\mathcal{Q}}{r_S} \int_0^{r_S} dr j_{\ell}(kr) \frac{(r - r_S)}{r} \ell(\ell + 1) (\check{\Phi} + \check{\Psi})(k, r) \\ &\quad + 2\mathcal{Q} \left(\frac{1}{r_S \mathcal{H}} - 1 \right) \int_0^{r_S} dr j_{\ell}(kr) (\check{\Phi}' + \check{\Psi}')(k, r) \\ &\quad + 2\mathcal{Q} \left(1 - \frac{1}{r_S \mathcal{H}} \right) \check{V}_m^{\parallel} \frac{\partial}{\partial(kr)} j_{\ell}(kr_S) \\ &\quad + 2\mathcal{Q} j_{\ell}(kr_S) \left\{ \check{\Psi} + \left(1 - \frac{1}{r_S \mathcal{H}} \right) \check{\Phi} \right\} \\ &\quad - \frac{2\mathcal{Q}}{r_S} \int_0^{r_S} dr j_{\ell}(kr) (\check{\Phi} + \check{\Psi})(k, r), \end{aligned} \quad (25)$$

where j_{ℓ} is the spherical Bessel function, and

$$\check{\Phi}(k, z) \equiv \Phi(k, z) / \Phi_d(k),$$

similarly for $\check{\Psi}$ and \check{V}_m^{\parallel} ; with Φ_d being the gravitational potential at the photon-matter decoupling epoch ($z = z_d$), given by

$$\Phi(k, z_d) = \frac{43}{50} \Phi_p(k) T(k) \equiv \Phi_d(k), \quad (26)$$

where $\Phi_p(k)$ is the primordial gravitational potential. Note that we have taken that, given the homogeneity and isotropy on large scales, galaxies flow with the underlying matter (i.e. they have similar velocity profile). We note that the first line in (25) gives the component for the “standard” angular power spectrum C_{ℓ}^{std} , which corresponds to (18).

We assume $w_{x,\text{eff}} = -1$, which allows the recovery of the well-known Λ CDM background at some epochs, and w_x as an absolute constant; by using (4), we have $\alpha_M \propto \Omega_x$. Thus, for all numerical computations, we use

$$w_{x,\text{eff}} = -1, \quad \alpha_M = \alpha_0 \Omega_x, \quad \alpha_0 \leq 0.6, \quad \mathcal{Q} = 1,$$

where α_0 is a constant (and we have $\alpha_0 \leq 0.6$ by imposing $w_{x0} \leq -0.8$). Evolutions are initialized at the photon-matter decoupling epoch $1 + z_d = 10^3 = 1/a(z_d)$, and use adiabatic initial conditions (see [2]) for the perturbations.

We also use a matter density parameter $\Omega_{m0} = 0.3$ and a Hubble constant $H_0 = 67.8 \text{ km} \cdot \text{s}^{-1} \cdot \text{Mpc}^{-1}$, from the Planck 2015 results [42]. Moreover, for the purpose of this work we take α_H and α_K as absolute constants, and we choose values of α_H such that we recover the same values of H_0 and Ω_{m0} ; with α_0 and α_K set to values that prohibit superluminal sound speeds, and also allow the recovery of luminal sound speeds at some epochs (see [2]). By the choice of the values of α_H , the magnification angular power spectra will match on small scales, at today ($z=0$) and any deviations that are solely owing to α_H will be isolated on the largest scales; at earlier epochs ($z > 0$) the angular power spectra will separate on all scales. Furthermore, given that the density of astrophysical objects decreases radially outwards from the centre so that $\Upsilon_1 > 0$ (< 0) corresponds to weakening (strengthening) gravity [2, 4], we use $\Upsilon_1 = 0.78$ and adopt a corresponding value for $\Upsilon_2 = -0.131$.

For qualitative purposes, as is the consideration in this work, we adopt an ideal case where cosmic variance is the only source of error in all computed quantities. The cosmic variance, is given by (e.g. [2, 27])

$$\sigma_\ell(z) = \sqrt{\frac{2}{(2\ell + 1)f_{\text{sky}}}} C_\ell(z), \quad (27)$$

where f_{sky} is the observed sky fraction. Here we adopted the value of an SKA-like survey, $f_{\text{sky}} = 0.75$. For practical purposes, proper quantitative methods and error (or noise) analysis will need to be taken into account.

In FIG. 1 we give the plots of the total magnification angular power spectrum (24) for the Horndeski parameter values $\alpha_H = 0.085, 0.1, 0.15$, with $\alpha_0 = 0.06$ and $\alpha_K = 0$: at the source redshifts $z_S = 0.5$ (top panel), $z_S = 1$ (middle panel), and $z_S = 3$ (bottom panel). We also indicate the associated extent of cosmic variance (27). We observe that, on scales $\ell \lesssim 20$, the amplitude of the angular power spectrum decreases as the source redshift increases; whereas, on smaller scales ($\ell > 20$), the amplitude increases as the source redshift increases. Moreover, the angular power spectrum for the different values of the Horndeski parameter gradually diverge on scales $\ell > 20$, as source redshift increases; with the separation becoming more prominent at $z_S \gtrsim 3$, for $\alpha_H > 0.085$. Furthermore, we see that the amplitude of the angular power spectrum increases with higher values of α_H , at all values of z_S and ℓ . This implies that cosmic magnification becomes enhanced (on all scales) as the strength of gravity increases. Thus, in beyond-Horndeski theory, stronger gravity regimes will induce stronger magnification events, while weaker gravity regimes induce (relatively) weaker magnification.

Moreover, the shaded regions in the plots of FIG. 1 show the extent of cosmic variance for the respective chosen values of the Horndeski parameter. As is already widely known, we see that cosmic variance becomes significant with increasing scale (decreasing ℓ) and increasing source redshift, encompassing the cosmic magnification signal in the angular power spectrum. This implies

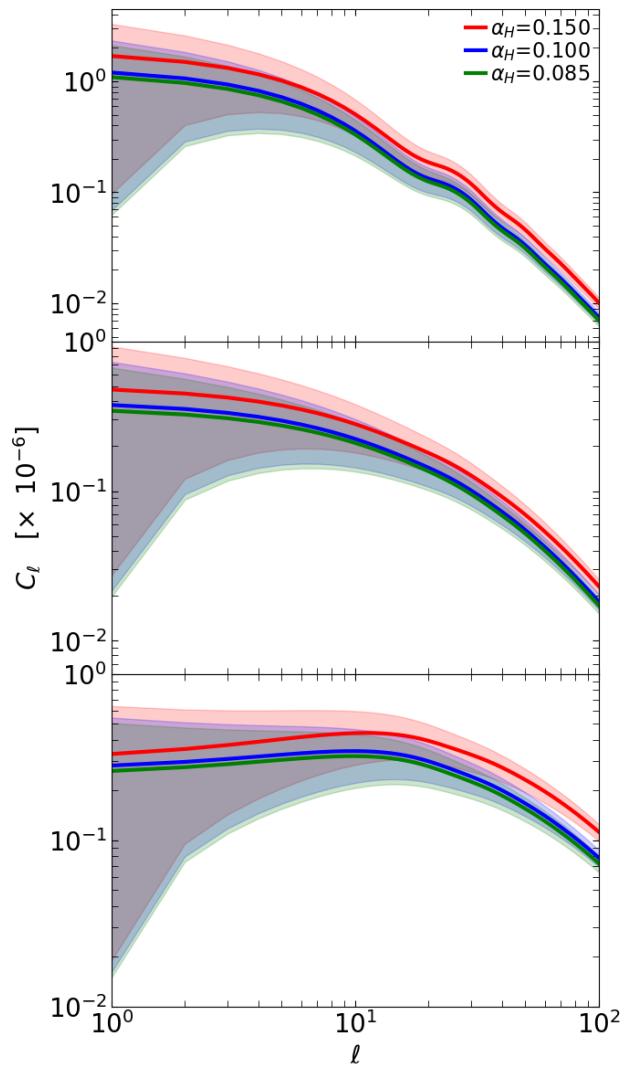


FIG. 1. The plots of the total magnification angular power spectrum C_ℓ as a function of multipole ℓ , at the source redshifts $z_S = 0.5$ (top), $z_S = 1.0$ (middle), and $z_S = 3.0$ (bottom): for the Horndeski parameter values $\alpha_H = 0.085, 0.1, 0.15$, accordingly; with the fixed parameter values, $\alpha_0 = 0.06$ and $\alpha_K = 0$. Shaded regions show the extent of cosmic variance.

that the cosmic magnification signal will ordinarily be overshadowed by cosmic variance in the analysis. Consequently, this signal will (in principle) not be observed on the largest scales, at the given source redshifts. However, by applying multi-tracer analysis (see e.g. [43–48]), the effect of cosmic variance can be subdued with large-volume, high-precision future surveys; thereby availing the possibility of detecting the magnification signal.

It should be pointed out that actual measurability of any signals will be subject to proper error analysis and other quantitative analyses, which will include several factors e.g. effectiveness and efficiency of the quantitative methods, survey specifications, and properties of the sources.

A. Imprint of UDE and total relativistic effect

Here we discuss the UDE imprint in the total (relativistic) magnification angular power spectrum (24). The focus is on highlighting the qualitative effect of UDE with respect to relativistic effects, on very large scales.

In FIG. 2, we show the plots of the fractional change $\Delta C_\ell/C_\ell^{\text{std}}$ in the total magnification angular power spectrum C_ℓ relative to the standard (weak-lensing) angular power spectrum C_ℓ^{std} , where $\Delta C_\ell = C_\ell - C_\ell^{\text{std}}$: for the same parameters as in FIG. 1; at the source redshifts $z_S = 0.5$ (top panel), $z_S = 1$ (middle panel), and $z_S = 3$ (bottom panel). The given fractions measure the total effect of relativistic corrections (20)–(23), i.e. the total relativistic signal, in the total magnification angular power spectrum for the given parameters and source redshifts. We also show the reach of cosmic variance (shaded regions). By using (27) and error propagation methods (e.g. [49, 50]), we have the cosmic variance for the total relativistic signal, given by

$$\sigma_\ell^{\text{rels}} = \frac{\sqrt{2}}{C_\ell^{\text{std}}} \sigma_\ell, \quad (28)$$

where σ_ℓ is as given by (27) (taking that C_ℓ and C_ℓ^{std} are uncorrelated). The $\sigma_\ell^{\text{rels}}$ regions in FIG. 2 are done with the least Horndeski parameter, $\alpha_H = 0.085$, at each z_S .

We see that on moving from high to low source redshift (bottom to top panel), the amplitude of the total relativistic signal in the total magnification angular power spectrum for each value of the Horndeski parameter increases. This implies that the amount of total relativistic signal in cosmic magnification will be higher at low source redshifts ($z_S < 1$) than at high source redshifts ($z_S \geq 1$), in beyond-Horndeski gravity. Similar results were previously found for interacting DE [13]. Moreover, the total relativistic signal gradually becomes significant, with respect to cosmic variance as source redshift decreases: at $z_S \geq 1$, the amplitude of the total relativistic signal is below cosmic variance on all scales; whereas, at $z_S = 0.5$ the amplitude of the total relativistic signal surpasses cosmic variance on scales $\ell \gtrsim 3$. Basically, this implies that at low source redshifts ($z_S \leq 0.5$) the total relativistic signal in cosmic magnification becomes directly measurable, with respect to cosmic variance; whereas, at high source redshifts ($z_S \geq 1$), multitracer techniques will be required to beat down cosmic variance. This suggests that cosmological surveys that depend on the apparent flux or angular size of sources, such as surveys of the baryon acoustic oscillation surveys of BOSS (e.g. [51]) and the 21 cm emission line of neutral hydrogen of the SKA (e.g. [52]) hold the potential to detect the total signal of non-lensing effects in the cosmic magnification, in beyond-Horndeski gravity, at low redshifts ($z < 1$). Also, this potentially reduces the need for higher technology (with high sensitivity and resolution) for conducting surveys at high redshifts, as wide-angle low-redshift surveys will be suitable.

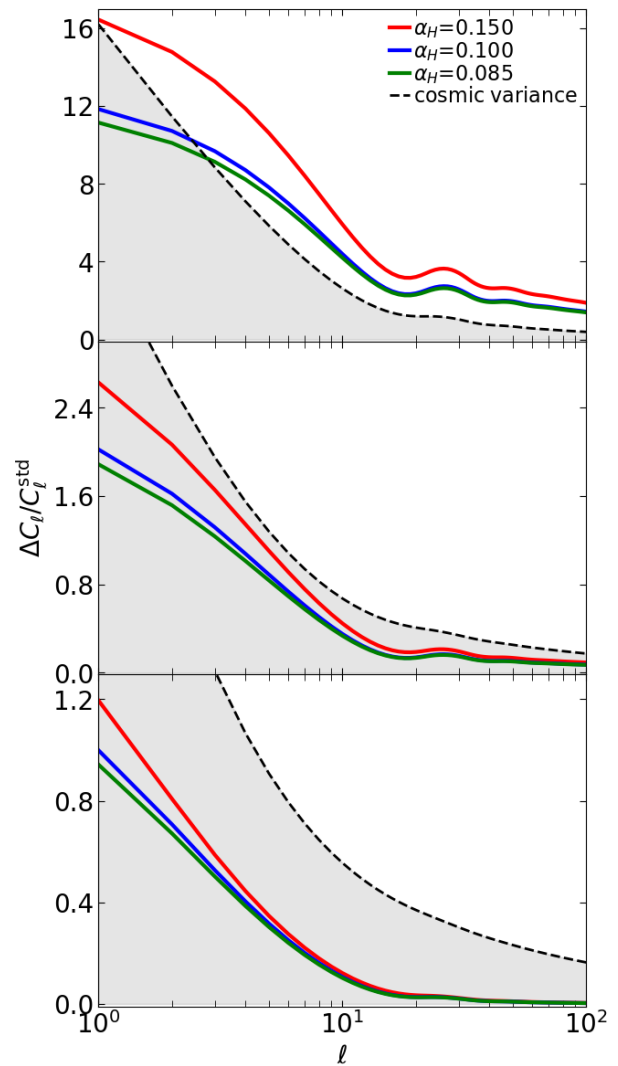


FIG. 2. The plots of the total relativistic signal in the magnification angular power spectrum C_ℓ : for the same parameters as in FIG. 1, at $z_S = 0.5$ (top), $z_S = 1.0$ (middle) and $z_S = 3.0$ (bottom), where we have $\Delta C_\ell = C_\ell - C_\ell^{\text{std}}$.

Furthermore, at each source redshift, we see that the amplitude of the total relativistic signal increases as the value of the Horndeski parameter increases. This implies that an increasing gravity strength in beyond-Horndeski gravity will lead to a boost or enhancement of the total relativistic signal. Moreover, the separation in the total relativistic signal for successive values of the Horndeski parameter increases with decreasing source redshift. In other words, the total relativistic signal for the various values of the Horndeski parameter become relatively better differentiated at lower source redshift. This shows that the signal of the combined relativistic effects is sensitive to small changes in UDE, and becomes more sensitive at lower redshifts. Thus, relativistic effects will be crucial in detecting the imprint of UDE, and possibly putting constraints on UDE, especially at later epochs.

B. Individual relativistic effects

In this section, we look at the contribution of the individual relativistic corrections (20)–(23), in the total magnification angular power spectrum.

We show in FIG. 3 the plots of the fractional change $\Delta\hat{C}_\ell/C_\ell^{(\text{no Doppler})}$ owing to the Doppler correction (20) in the total magnification angular power spectrum C_ℓ , as a function of ℓ , where we have $\Delta\hat{C}_\ell = C_\ell - C_\ell^{(\text{no Doppler})}$. The plots are given at $z_S = 0.5$ (top panel), $z_S = 1$ (middle panel), and $z_S = 3$ (bottom panel): for the Horndeski parameter values $\alpha_H = 0.085, 0.1, 0.15$, accordingly; with $\alpha_0 = 0.06$ and $\alpha_K = 0$. These fractions measure the Doppler signal in the total magnification angular power spectrum for the given Horndeski parameter values, at the given source redshifts. We see that at each z_S , as the value of the Horndeski parameter increases, the amplitude of the magnification Doppler signal also increases: at $z_S > 0.5$ the growth in amplitude appears to occur on all scales; whereas, at $z_S = 0.5$ the growth occurs on scales $\ell \lesssim 20$, while on scales $\ell > 20$ the behaviour of the magnification Doppler signal reverses, where an increasing $\alpha_H \geq 0.15$ will lead to a decreasing amplitude of the magnification Doppler signal. This implies that stronger UDE ($\alpha_H \geq 0.15$), and hence beyond-Horndeski gravity, will enhance the signal of Doppler effect in the magnification of cosmic objects on all scales at earlier epochs ($z_S > 0.5$), and only on the largest scales ($\ell \lesssim 20$) at late-time epochs ($z_S \leq 0.5$).

We also show the extent of the cosmic variance (shaded regions) for the magnification Doppler signal. For any individual relativistic signal X , the associated cosmic variance (by similar calculations as for $\sigma_\ell^{\text{rels}}$), is given by

$$\sigma_\ell^X = \frac{\sqrt{2}}{C_\ell^{(\text{no } X)}} \sigma_\ell, \quad (29)$$

where σ_ℓ is as given by (27); with $X = \text{Doppler, ISW, time-delay, potential}$: σ_ℓ^X applies to FIGS. 3–6. Similarly, as in FIG. 2, the given regions for cosmic variance (29) in FIGS. 3–6 are for $\alpha_H = 0.085$. In FIG. 3, by going from the bottom to the top panel (direction of decreasing z_S), we notice the behaviour of the magnification Doppler signal with respect to cosmic variance: a gradual growth in amplitude as source redshift decreases. We see the magnification Doppler signal gradually surpasses the cosmic variance, at $z_S \lesssim 0.5$. Thus, this implies that (in principle) the Doppler signal in the total magnification angular power spectrum is potentially measurable without the need of multi-tracer analysis, at the given z_S . Moreover, we see that the separation in the magnification Doppler signal between successive values of the Horndeski parameter increases as source redshift decreases: albeit not obvious for the separation between the red line ($\alpha_H = 0.085$) and blue line ($\alpha_H = 0.1$) at $z_S = 0.5$, which is overshadowed by the separation between the blue line and the green line ($\alpha_H = 0.15$). (The separation between the blue line and the green line is ~ 0.01 at $z_S = 3$, ~ 0.1

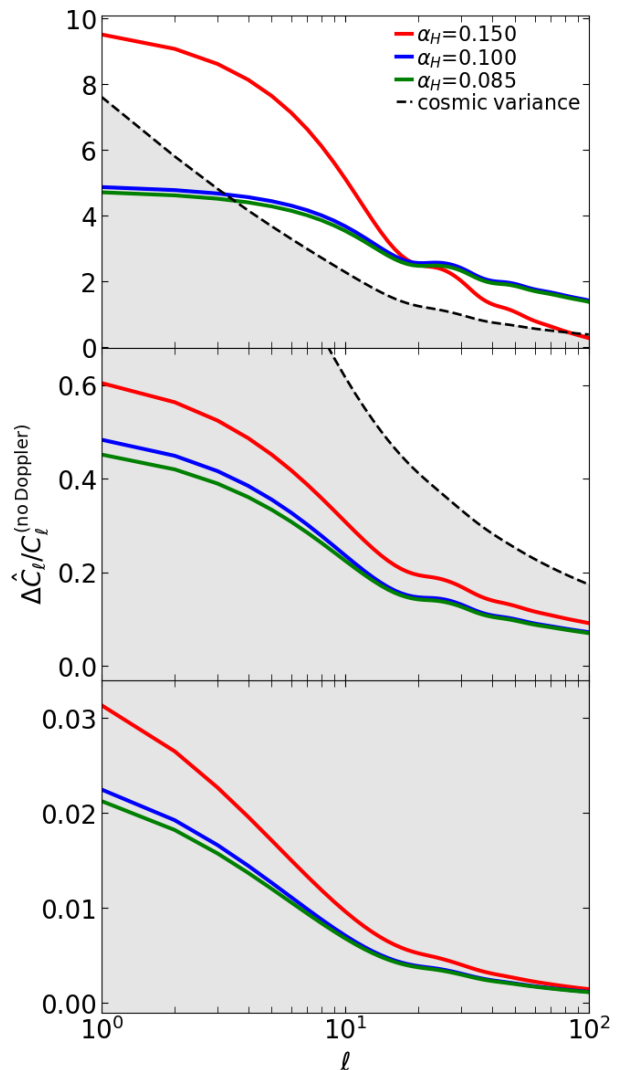


FIG. 3. The plots of Doppler signal in the total magnification angular power spectrum C_ℓ : for the same parameters as in FIG. 1, at $z_S = 0.5$ (top), $z_S = 1.0$ (middle), and $z_S = 3.0$ (bottom), where we have $\Delta\hat{C}_\ell = C_\ell - C_\ell^{(\text{no Doppler})}$.

at $z_S = 1$, and ~ 4 at $z_S = 0.5$.) Although the values of the separation seem marginal for $\alpha_H < 0.15$, they nevertheless show that the magnification Doppler signal is relatively more sensitive to changes in UDE at low source redshift ($z_S \lesssim 0.5$). This implies that the Doppler signal in the total magnification angular power spectrum holds the potential of measuring the imprint of UDE, at the given source redshift.

FIG. 3 also shows that the amplitude of the magnification Doppler signal decreases as source redshift increases (top to bottom panels). Therefore, magnification of sources owing to peculiar velocities diminishes at larger cosmic distances. It should be pointed out that the apparent oscillations (on scales $20 \lesssim \ell \lesssim 60$, at $z_S \lesssim 1$) in the magnification Doppler signal (and other signals), are likely to be from the Bessel spherical function, which

tends to dominate the magnification power spectrum amplitude. Essentially, we see that the behaviour and amplitude of the total relativistic signal in the total magnification angular power spectrum, at $z_S \lesssim 0.5$ (FIG. 2, top panel) follows that of the Doppler signal, indicating that it is prescribed by the Doppler signal at the given source redshift.

In FIG. 4 we show the plots of the fractional change $\Delta\hat{C}_\ell/C_\ell^{(\text{no ISW})}$ owing to the ISW correction (21) in the total magnification angular power spectrum (24), as a function of ℓ , where $\Delta\hat{C}_\ell = C_\ell - C_\ell^{(\text{no ISW})}$. The plots are given at $z_S = 0.5$ (top panel), $z_S = 1$ (middle panel), and $z_S = 3$ (bottom panel): for the Horndeski parameter values $\alpha_H = 0.085, 0.1, 0.15$, accordingly; with $\alpha_0 = 0.06$ and $\alpha_K = 0$. Similarly, we show the extent of cosmic variance (shaded regions), as given by (29). These fractions measure the ISW signal in the total magnification angular power spectrum for the given Horndeski parameter values, at the given source redshifts. In comparison to the magnification Doppler signal (FIG. 3), we see that the magnification ISW signal also grows as ℓ increases, with the signal for the various values of the Horndeski parameter diverging on larger scales (smaller ℓ) and converging on smaller scales (larger ℓ); except that there are relatively larger separations in the magnification ISW signal for the different values of the Horndeski parameter than in the magnification Doppler signal on smaller scales, at each given source redshifts.

Moreover, we see a gradual growth in amplitude in the magnification ISW signal as source redshift increases: at $z_S < 3$ the magnification ISW signal is subdued by cosmic variance on all scales; whereas, at $z_S = 3$, the magnification ISW signal grows and surpasses cosmic variance for $\alpha_H \geq 0.1$, on all scales. (The growth in amplitude with increase in z_S is understandable since the ISW effect is an integral effect, which will increase with redshift or distance.) Thus, the ISW signal in the total magnification angular power spectrum is potentially measurable directly for relatively large amplitudes of the Horndeski parameter ($\alpha_H \gtrsim 0.1$), at high source redshifts ($z_S \geq 3$); whereas, at lower source redshifts ($z_S < 3$), multi-tracer techniques will be needed. Although in this work we have assumed that the Horndeski parameter is an absolute constant, in general it evolves with time and hence, can grow to large amplitudes as given here (or even larger).

Furthermore, we see that the separation in the ISW signal in the total magnification angular power spectrum appear to be largest at $z_S = 3$, indicating that the magnification ISW signal is relatively more sensitive to changes in UDE at high source redshift ($z_S \geq 3$). This implies that the ISW signal in the total magnification angular power spectrum holds the potential of detecting the imprint of UDE, at larger cosmic distances (higher redshifts).

Similarly, in FIG. 5 we show the plots of the fractional change $\Delta\hat{C}_\ell/C_\ell^{(\text{no timedelay})}$ owing to the time-delay correction (22) in the total magnification angular power spectrum C_ℓ , where we have $\Delta\hat{C}_\ell = C_\ell - C_\ell^{(\text{no timedelay})}$.

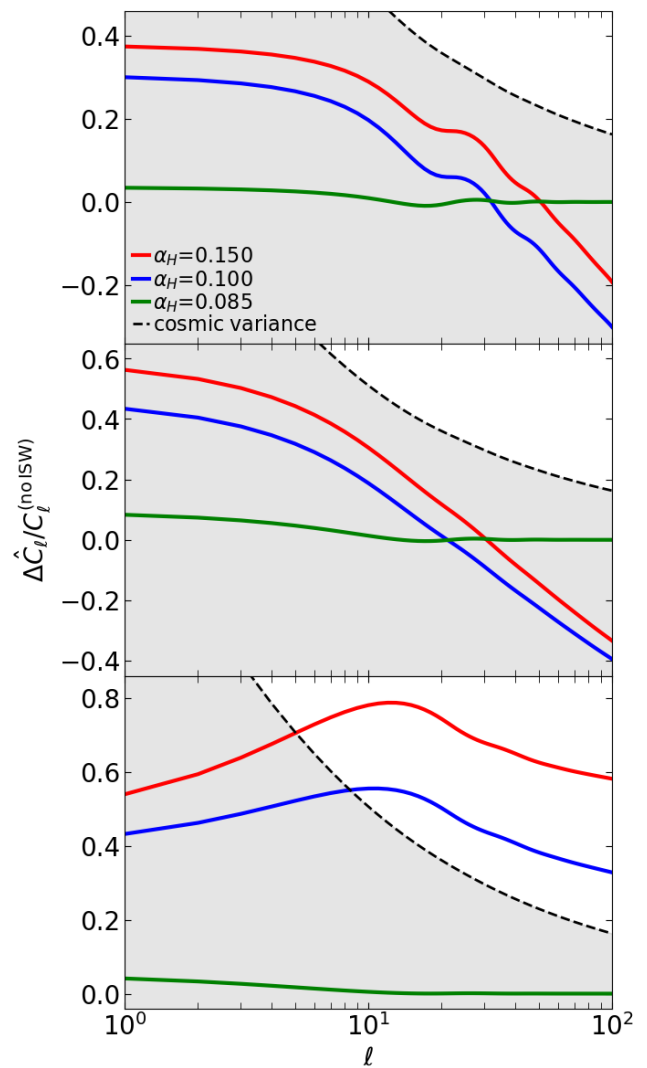


FIG. 4. The plots of ISW signal in the total magnification angular power spectrum C_ℓ : for the same parameters as in FIG. 1, at $z_S = 0.5$ (top), $z_S = 1.0$ (middle), and $z_S = 3.0$ (bottom), where we have $\Delta\hat{C}_\ell = C_\ell - C_\ell^{(\text{no ISW})}$.

The plots are given at $z_S = 0.5$ (top panel), $z_S = 1$ (middle panel), and $z_S = 3$ (bottom panel): for the Horndeski parameter values $\alpha_H = 0.085, 0.1, 0.15$, accordingly; with $\alpha_0 = 0.06$ and $\alpha_K = 0$. Also, we show the extent of cosmic variance (shaded regions), as given by (29). These fractions measure the time-delay signal in the total magnification angular power spectrum for the chosen Horndeski parameter values, at the given source redshifts. We see that at $z_S < 3$, the behaviour of the magnification time-delay signal is similar to that of the magnification ISW signal (FIG. 4, middle and top panels), except that the amplitude of the magnification time-delay signal is larger; whereas at $z_S = 3$, the behaviour of the magnification time-delay signal appears to resemble the inverse of the magnification ISW signal somewhat (for $\alpha_H \geq 0.1$). The magnification time-delay signal also shows potential

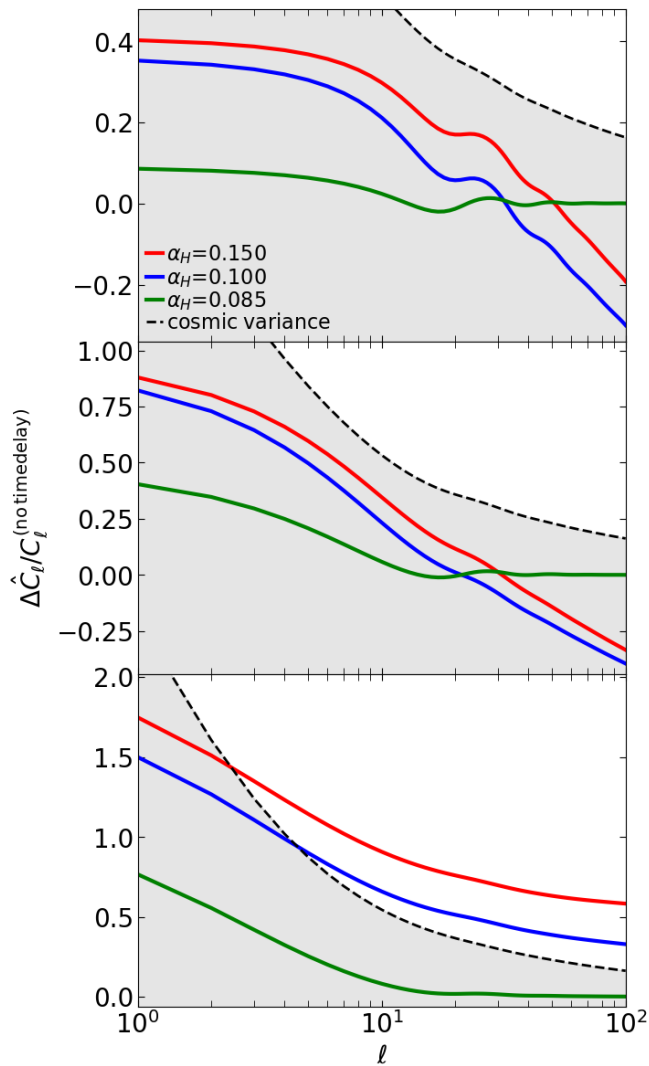


FIG. 5. The plots of time-delay signal in the total magnification angular power spectrum C_ℓ : for the same parameters as in FIG. 1, at $z_S = 0.5$ (top), $z_S = 1.0$ (middle), and $z_S = 3.0$ (bottom), where we have $\Delta\hat{C}_\ell = C_\ell - C_\ell^{(\text{no timedelay})}$.

of measurability at $z_S \geq 3$. Similar to the magnification ISW signal, the observed growth in amplitude with increase in z_S in the magnification time-delay signal is related to the fact that time delay is an integral effect, which will increase with redshift. Essentially, from the results it implies that it will be possible to measure the magnification time-delay signal at high source redshifts ($z_S \geq 3$) without the need for multi-tracer techniques.

Moreover, we see that the separation in the time-delay signal in the total magnification angular power spectrum for $\alpha_H \geq 0.1$ increases with increase in source redshift, with the largest separation occurring at $z_S = 3$. This suggests that the magnification time-delay signal is relatively more sensitive to changes in UDE at high source redshift. Thus, the time-delay signal in the total magnification angular power spectrum holds the potential to detect the

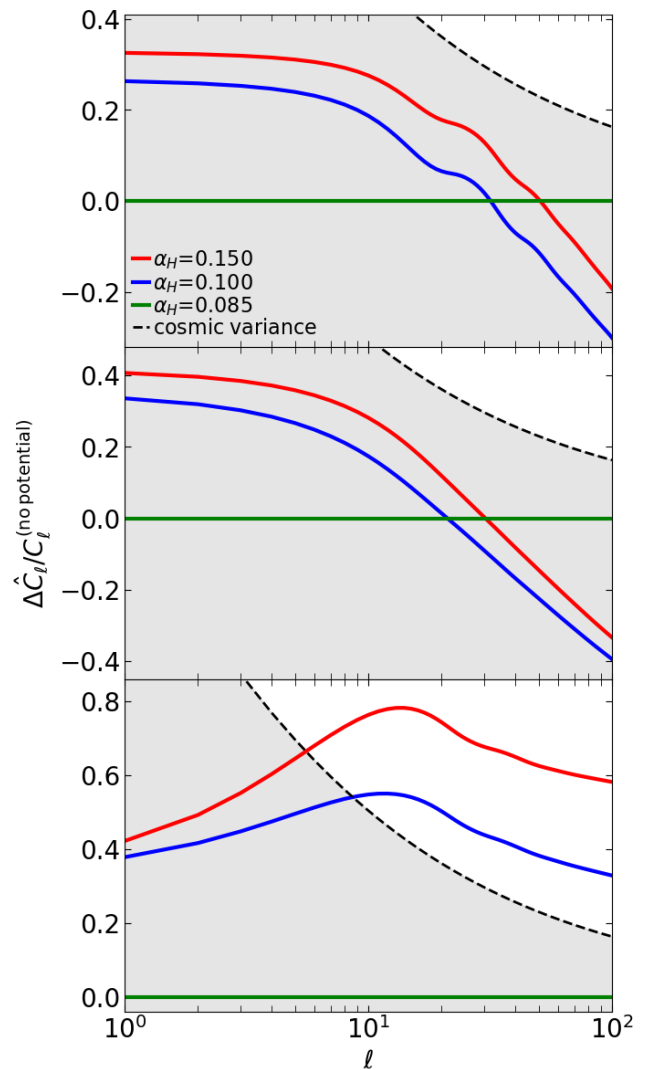


FIG. 6. The plots of (gravitational) potential signal in the total magnification angular power spectrum C_ℓ : for the same parameters as in FIG. 1, at the source redshifts $z_S = 0.5$ (top), $z_S = 1.0$ (middle), and $z_S = 3.0$ (bottom), where we have $\Delta\hat{C}_\ell = C_\ell - C_\ell^{(\text{no potential})}$.

UDE imprint, at $z_S \geq 3$.

In FIG. 6 we show the plots of the fractional change $\Delta\hat{C}_\ell/C_\ell^{(\text{no potential})}$ owing to the gravitational potential correction (23) in the total magnification angular power spectrum C_ℓ , where $\Delta\hat{C}_\ell = C_\ell - C_\ell^{(\text{no potential})}$. The plots are given at $z_S = 0.5$ (top panel), $z_S = 1$ (middle panel), and $z_S = 3$ (bottom panel): for the Horndeski parameter values $\alpha_H = 0.085, 0.1, 0.15$, accordingly; with $\alpha_0 = 0.06$ and $\alpha_K = 0$. We also show the extent of cosmic variance (shaded regions), as given by (29). These fractions measure the (gravitational) potential signal in the total magnification angular power spectrum for the given Horndeski parameter values, at the given source redshifts. We see that the behaviour of the magnification potential signal is similar to that of the magnification

ISW signal, at the given source redshifts, except that the amplitude of the magnification potential signal at the given source redshifts is relatively lower. Thus, similar discussion follow for the magnification potential signal (as for the magnification ISW signal). Moreover, the magnification potential signal appear to tend to vanish for smaller Horndeski parameter values ($\alpha_H \lesssim 0.085$), as opposed to the corresponding magnification ISW signal for the same Horndeski parameter values (the same for the magnification time-delay signal). This is understandable since the magnification ISW and the time-delay signals, respectively, are sourced by integral effects, whose amplitude will accumulate over cosmological distances; on the other hand, the magnification potential signal is sourced by local (non-integral) gravitational potential-well effects that are independent of distance, and hence will grow relatively much slower.

In general, the results show that the Doppler signal dominates at low redshifts ($z \lesssim 0.5$) while the ISW, the time-delay, and the potential signals, respectively, dominate at high redshifts ($z \gtrsim 3$). For completeness we give the associated signal-to-noise ratios for all signals in §V.

V. SIGNAL-TO-NOISE RATIO

Here we consider a (theoretical) signal-to-noise ratio (S/N) for results discussed in §IV A and §IV B. As previously stated, for the purpose of this work we only consider S/N with respect to cosmic variance. The estimations of S/N will help in shading light on the possibility of detecting the magnification signals in observational data.

By using $\sigma_\ell^{\text{rels}}$ (28), we obtain the S/N for the total relativistic signal in the total magnification angular power spectrum (FIG. 2), given by

$$\left(\frac{S}{N}\right)_\ell^{\text{rels}} = \frac{1}{2} \sqrt{(2\ell + 1)f_{\text{sky}}} \left(1 - \frac{C_\ell^{\text{std}}}{C_\ell}\right), \quad (30)$$

where C_ℓ^{std} and C_ℓ are as given in §IV. For detection, we need $(S/N)_\ell^{\text{rels}} > 1$.

In FIG. 7, we show the plots of the signal-to-noise ratio $(S/N)_\ell^{\text{rels}}$ of the total relativistic signal in the total magnification angular power spectrum (see FIG. 2), as a function of multipole ℓ : at $z_S = 0.5$ (top panel), $z_S = 1.0$ (middle panel), and $z_S = 3.0$ (bottom panel), for $\alpha_H = 0.085, 0.1, 0.15$, accordingly; with $\alpha_0 = 0.06$ and $\alpha_K = 0$. We see that, at $z_S = 0.5$, we have $(S/N)_\ell^{\text{rels}} > 1$ and increases on scales $\ell \gtrsim 3$; whereas, at $z_S \geq 1$, we have $(S/N)_\ell^{\text{rels}} \leq 1$. Thus, this suggests that the potential of direct detection of the total relativistic signal in the total magnification angular power spectrum with observational data occurs at low redshifts ($z < 1$); whereas at higher redshifts ($z \geq 1$), surveys will require multi-tracer techniques, to beat down cosmic variance. This is consistent with the results in §IV A (see FIG. 3).

Similarly, by using σ_ℓ^X (29), we obtain the S/N for the individual relativistic signals in the total magnification

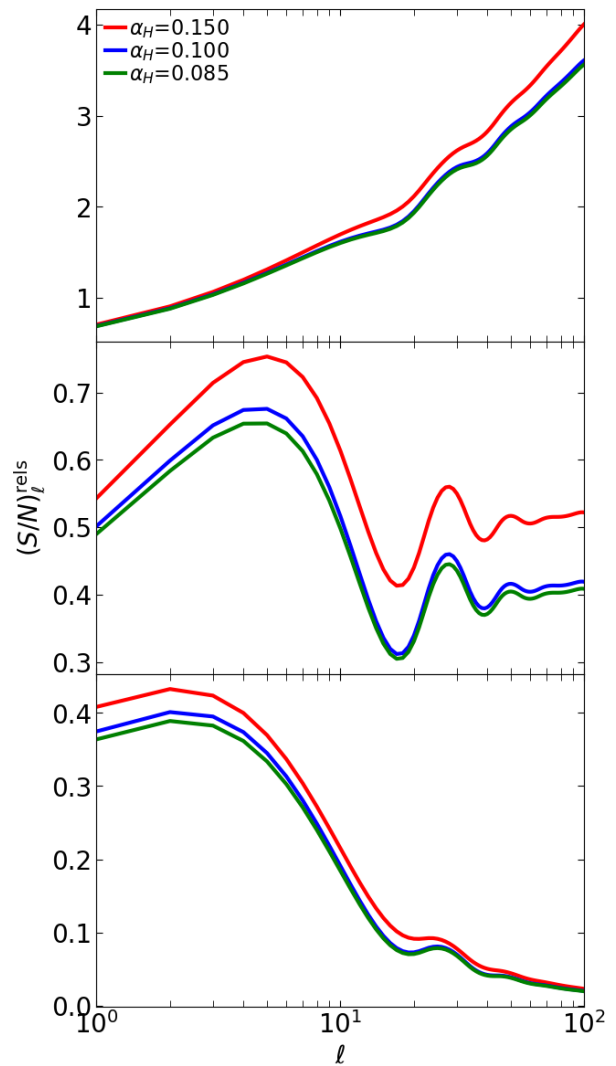


FIG. 7. The plots of the signal-to-noise ratio of the total relativistic signal in the total magnification angular power spectrum C_ℓ : for the same parameters as in FIG. 2, at $z_S = 0.5$ (top), $z_S = 1.0$ (middle), and $z_S = 3.0$ (bottom).

angular power spectrum (see FIGs. 3–6), given by

$$\left(\frac{S}{N}\right)_\ell^X = \frac{1}{2} \sqrt{(2\ell + 1)f_{\text{sky}}} \left(1 - \frac{C_\ell^{(\text{no X})}}{C_\ell}\right), \quad (31)$$

where $C_\ell^{(\text{no X})}$ and C_ℓ are as given in §IV; with X denoting the individual relativistic signals. Basically, $(S/N)_\ell^X$ is a generalisation of $(S/N)_\ell^{\text{rels}}$ (just as σ_ℓ^X generalises $\sigma_\ell^{\text{rels}}$). Then for detection of the signals, we need $(S/N)_\ell^X > 1$.

We show in FIG. 8, the plots of the signal-to-noise ratio $(S/N)_\ell^{\text{Doppler}}$ of the Doppler signal in the total magnification angular power spectrum (see FIG. 3), as a function of multipole ℓ : at $z_S = 0.5$ (top panel), $z_S = 1.0$ (middle panel), and $z_S = 3.0$ (bottom panel), for $\alpha_H = 0.085, 0.1, 0.15$, accordingly; with $\alpha_0 = 0.06$ and $\alpha_K = 0$. We see that, at $z_S = 0.5$, $(S/N)_\ell^{\text{Doppler}} > 1$ and

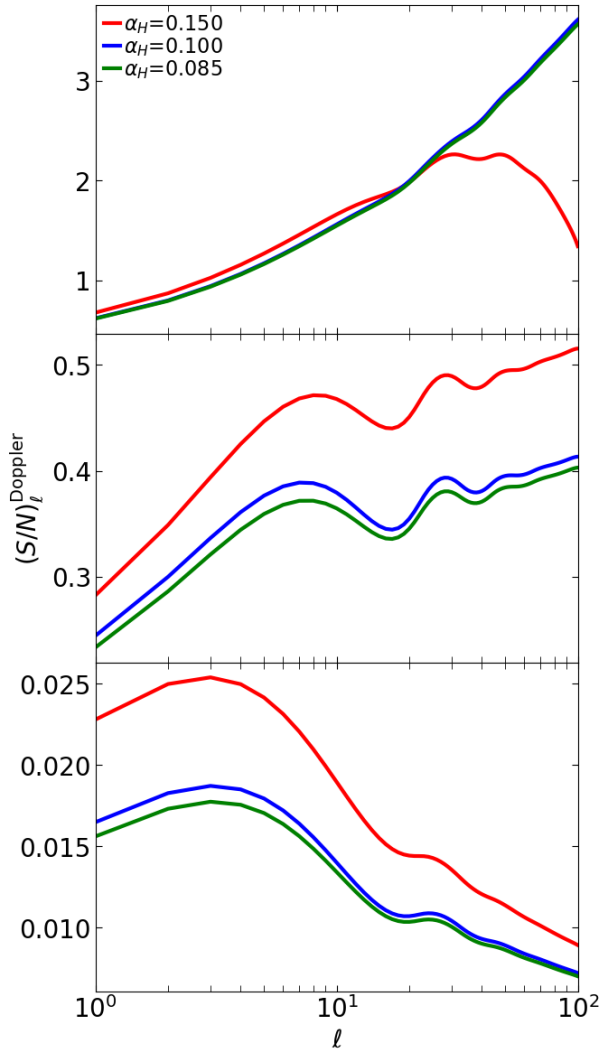


FIG. 8. The plots of the signal-to-noise ratio of Doppler signal in the total magnification angular power spectrum C_ℓ : for the same parameters as in FIG. 3, at $z_S = 0.5$ (top), $z_S = 1.0$ (middle), and $z_S = 3.0$ (bottom).

increases on scales $\ell \gtrsim 3$ for $\alpha_H < 0.15$ —with that of $\alpha_H = 0.15$ decreasing on scales $\ell > 20$; whereas, at $z_S \geq 1$, we have $(S/N)_\ell^{\text{Doppler}} \leq 1$. The behaviour of $(S/N)_\ell^{\text{Doppler}}$ for $\alpha_H = 0.15$, at $z_S = 0.5$, can be understood from the behaviour of the magnification Doppler signal in §IV B (see FIG. 3), at the given z_S : the amplitude of the magnification Doppler signal for $\alpha_H = 0.15$ diminishes relative to that of lower values of α_H , on scales $\ell \gtrsim 20$. The behaviour of $(S/N)_\ell^{\text{Doppler}}$ suggests that there is a potential of direct detection of the magnification Doppler signal with observational data at low redshifts ($z \lesssim 0.5$); whereas at higher redshifts ($z \geq 1$), multi-tracer techniques will need to be taken into account, to beat down cosmic variance. This is consistent with the results in §IV B. The behaviour of $(S/N)_\ell^{\text{Doppler}}$ for $\alpha_H = 0.15$ at $z_S = 0.5$, may be an indication that the occurrence of

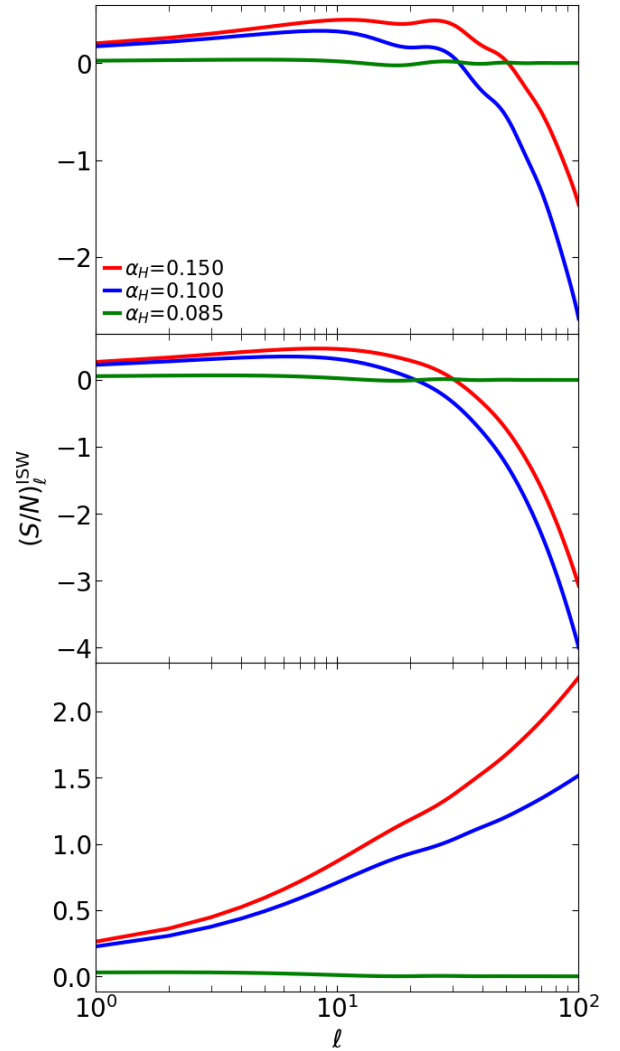


FIG. 9. The plots of the signal-to-noise ratio of ISW signal in the total magnification angular power spectrum C_ℓ : for the same parameters as in FIG. 4, at $z_S = 0.5$ (top), $z_S = 1.0$ (middle), and $z_S = 3.0$ (bottom).

magnification Doppler effect in beyond-Horndeski gravity rather requires a relatively weaker gravity regions or regime ($\alpha_H < 0.15$), on scales $\ell > 20$.

In FIG. 9, we show the plots of the signal-to-noise ratio $(S/N)_\ell^{\text{ISW}}$ of the ISW signal in the total magnification angular power spectrum (see FIG. 4), as a function of multipole ℓ : at $z_S = 0.5$ (top panel), $z_S = 1.0$ (middle panel), and $z_S = 3.0$ (bottom panel), for $\alpha_H = 0.085, 0.1, 0.15$, accordingly; with $\alpha_0 = 0.06$ and $\alpha_K = 0$. We see that at $z_S < 3$ we have $(S/N)_\ell^{\text{ISW}} \leq 1$, and at $z_S = 3$, we have $(S/N)_\ell^{\text{ISW}} > 1$ and increases for $\alpha_H \geq 0.1$ on scales $\ell \gtrsim 10$. This suggests that the potential of direct detection of the ISW signal in the total magnification angular power spectrum with observational data occurs at high redshifts ($z \geq 3$); whereas at lower redshifts ($z < 3$), surveys will require multi-tracer techniques, to beat down cosmic variance. This is consistent with the results in §IV B

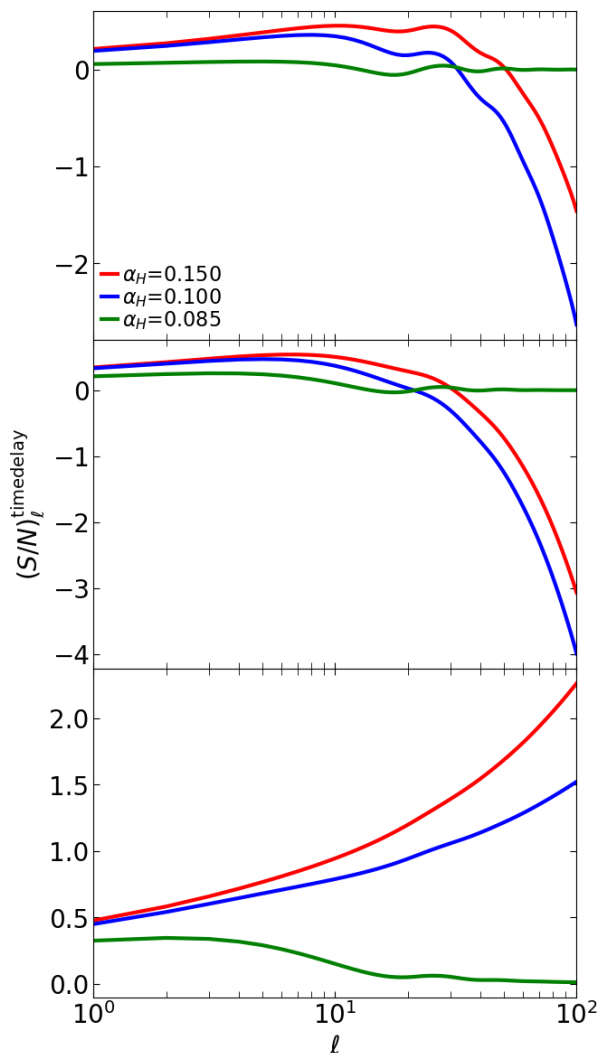


FIG. 10. The plots of the signal-to-noise ratio of time-delay signal in the total magnification angular power spectrum C_ℓ : for the same parameters as in FIG. 5, at $z_S = 0.5$ (top), $z_S = 1.0$ (middle), and $z_S = 3.0$ (bottom).

Similarly, in FIG. 10 we show the plots of the signal-to-noise ratio $(S/N)_\ell^{\text{timedelay}}$ of the time-delay signal in the total magnification angular power spectrum (see FIG. 5), as a function of multipole ℓ : at $z_S = 0.5$ (top panel), $z_S = 1.0$ (middle panel), and $z_S = 3.0$ (bottom panel), for $\alpha_H = 0.085, 0.1, 0.15$, accordingly; with $\alpha_0 = 0.06$ and $\alpha_K = 0$. We see that we have $(S/N)_\ell^{\text{timedelay}} \leq 1$ at $z_S < 3$; whereas, at $z_S = 3$ we have $(S/N)_\ell^{\text{timedelay}} > 1$ and increases on scales $\ell \gtrsim 10$ for $\alpha_H \gtrsim 0.1$. (This is similar to $(S/N)_\ell^{\text{ISW}}$.) This suggests that observational data at high redshifts ($z \geq 3$) hold the potential to detect the time-delay signal in the total magnification angular power spectrum directly for strong gravity regimes, but at low redshifts ($z < 3$) observational analyses will require multi-tracer techniques to beat down cosmic variance. This is consistent with the results in §IV B (see FIG. 5).

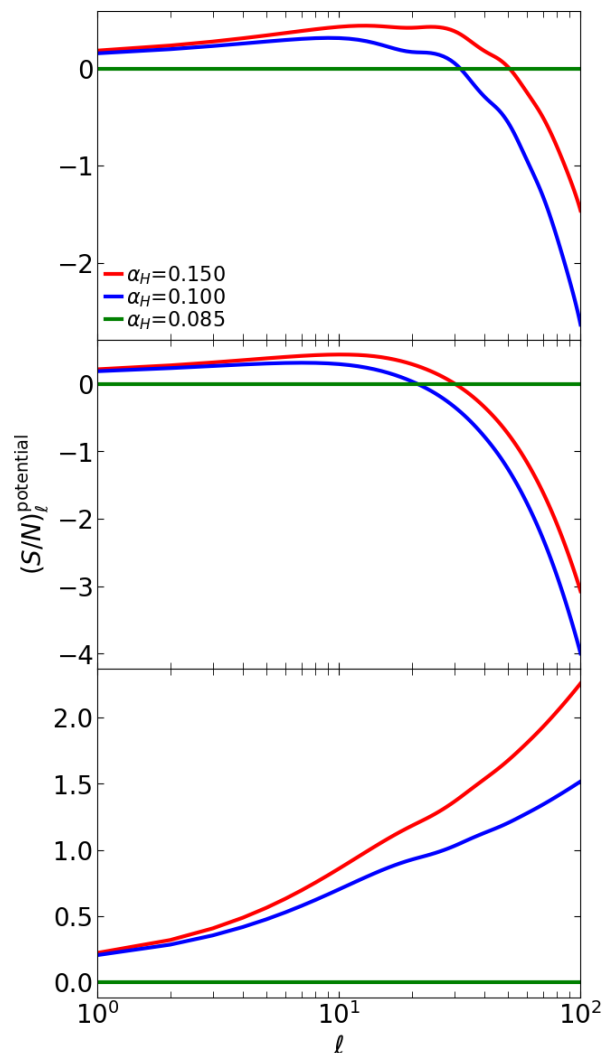


FIG. 11. The plots of the signal-to-noise ratio of (gravitational) potential signal in the total magnification angular power spectrum C_ℓ : for the same parameters as in FIG. 6, at $z_S = 0.5$ (top), $z_S = 1.0$ (middle), and $z_S = 3.0$ (bottom).

In FIG. 11, we show the plots of the signal-to-noise ratio $(S/N)_\ell^{\text{potential}}$ of the (gravitational) potential signal in the total magnification angular power spectrum (see FIG. 6), as a function of multipole ℓ : at $z_S = 0.5$ (top panel), $z_S = 1.0$ (middle panel), and $z_S = 3.0$ (bottom panel), for $\alpha_H = 0.085, 0.1, 0.15$, accordingly; with $\alpha_0 = 0.06$ and $\alpha_K = 0$. We see that we have almost identical results as for $(S/N)_\ell^{\text{timedelay}}$, except that for $\alpha_H = 0.085$ the magnification potential signal-to-noise ratio vanishes, $(S/N)_\ell^{\text{potential}} = 0$ at all z_S . Moreover, this is consistent with the results in §IV B (see FIG. 4). Thus, similar deductions as for $(S/N)_\ell^{\text{timedelay}}$ follow.

It appears that at $z_S \geq 3$, the ISW, the time-delay, and the potential signals, respectively, will prefer stronger gravity regimes ($\alpha_H \gtrsim 0.1$) with respect to cosmic variance, since otherwise the signals are diminished.

VI. CONCLUSION

We presented a qualitative analysis of cosmic magnification in the beyond-Horndeski gravity, via the unified dark energy model. We used the angular power spectrum for our analysis. We set the effective equation of state parameter of the given unified dark energy to a value which allows the recovery of the background cosmology of the well-known Λ CDM model, at some epochs. Moreover, for simplicity, the Horndeski parameter was taken as an absolute constant (but in general, would depend on time and hence able to grow to different amplitudes): the chosen values were such that the same values of H_0 and Ω_{m0} were obtained. This ensured that any deviations in the magnification angular power spectrum that are solely owing to the perturbations in the unified dark energy (hence, beyond-Horndeski gravity) were isolated on large scales.

We discussed the imprint of unified dark energy and the total (relativistic) magnification angular power spectrum. We investigated the total signal of relativistic effects, and the signal of the individual relativistic effects, in the total magnification angular power spectrum. Furthermore, we estimated the (theoretical) signal-to-noise ratio of various magnification signals. For the purpose of this work, we only consider cosmic variance as the source of error.

Our results showed that in the beyond-Horndeski theory, strong gravity regimes will induce strong cosmic magnification events, and vice versa. Moreover, we found that a multi-tracer analysis (e.g. [43–48]) will be needed to beat down cosmic variance, in order to increase the possibility of detecting the signal of the total (relativistic) magnification, in a universe governed by beyond-Horndeski gravity. The magnification signal will ordinarily be overshadowed by cosmic variance on very large scales, and hence will not be observed. However, if two or more tracers of the matter distribution in the same volume are used (the multi-tracer framework), the effect of cosmic variance can be suppressed; thereby allowing the possible detection of the magnification signal. Thus, in the light of multi-tracer analysis, future large-volume, high-precision surveys hold the potential to measure cosmic magnification.

We also found that the total relativistic signal in the cosmic magnification is potentially measurable directly at redshifts $z < 1$. However, at higher redshifts ($z \geq 1$), multi-tracer analysis will be required to subdue cosmic variance on scales $\ell > 3$. This suggests that magnification surveys (e.g. cosmological surveys that measure angular size of sources), at redshifts $z < 1$, hold the potential to detect the total signal of relativistic effects in the cosmic magnification in beyond-Horndeski gravity.

The results showed that the unified dark energy, and hence beyond-Horndeski gravity, can enhance the signal of Doppler effect in the cosmic magnification on all scales at earlier epochs ($z > 0.5$), and only on the largest scales ($\ell \lesssim 20$) at late-time epochs ($z \leq 0.5$). In essence,

in beyond-Horndeski theory, regions of stronger gravity will have higher magnification Doppler signal than regions with relatively weaker gravity. The results also suggested that the Doppler signal in the total magnification angular power spectrum is measurable (with respect to cosmic variance) at low redshifts ($z < 0.5$), without the need for multi-tracer analysis. Moreover, the signal of Doppler effect in the total magnification angular power spectrum holds the potential of detecting the imprint of unified dark energy.

Furthermore, unlike in the magnification Doppler signal where the amplitude increased with decreasing redshift, the amplitude of the magnification ISW signal increased with increasing redshift. We found that the magnification ISW signal is potentially measurable directly, for relatively large amplitudes of the Horndeski parameter ($\alpha_H \geq 0.1$), at high redshifts ($z \geq 3$). On the other hand, at lower redshifts ($z < 3$), a multi-tracer analysis will be needed, for scales $\ell \gtrsim 20$. We also found that, the magnification ISW signal holds the potential to detect the imprint of unified dark energy, at high redshifts ($z \geq 3$). The same conclusion follows for the magnification time-delay signal. (This is understandable since both signals are sourced by integral effects.) In general, relativistic effects are sensitive to small changes in unified dark energy: this will be crucial in detecting the imprint of beyond-Horndeski gravity in the total magnification angular power spectrum.

The results showed that the magnification Doppler signal will dominate in the beyond-Horndeski gravity, at low redshifts ($z \lesssim 0.5$); whereas, the ISW, the time-delay, and potential signals, respectively, will dominate at high redshifts ($z \gtrsim 3$). Moreover, we found that the ISW, the time-delay, and the potential signals, respectively, will have the same signal-to-noise ratio at redshifts $z \geq 3$, and hence the same potential of detectability in observational data, at the given redshifts. Furthermore, the results suggested that the magnification Doppler signal in beyond-Horndeski gravity will prefer a relatively weaker gravity regime ($\alpha_H < 0.15$), and the other signals will prefer stronger gravity regimes ($\alpha_H \gtrsim 0.1$).

ACKNOWLEDGMENTS

We thank the Centre for High Performance Computing (CHPC), Cape Town, South Africa, for providing the computing facilities with which all the numerical computations in this work were done.

Appendix A: The Cosmological Equations

The equations given in this appendix are drawn from the works by [1] and [2].

1. The perturbations equations

The gravitational potential are given, via the metric (5), by

$$\Phi \equiv \delta N + \mathcal{H}\Pi + \Pi', \quad \Psi \equiv -\zeta - \mathcal{H}\Pi, \quad \Pi = a\psi, \quad (\text{A1})$$

where ψ is a metric scalar potential, δN is the metric temporal perturbation, and ζ is a metric spatial potential. The evolutions of the UDE momentum density and (energy) density perturbation—which were used in obtaining (15) and (16)—are given by

$$q'_x + 4\mathcal{H}q_x + (\bar{\rho}_x + \bar{p}_x)\Phi + \delta p_x - \frac{2}{3}k^2\sigma_x = \alpha_M\mathcal{H}q, \quad (\text{A2})$$

$$\delta\rho'_x + 3\mathcal{H}(\delta\rho_x + \delta p_x) - 3(\bar{\rho}_x + \bar{p}_x)\Psi' - k^2q_x = \alpha_M\mathcal{H}\delta\rho, \quad (\text{A3})$$

where $q_A = (\bar{\rho}_A + \bar{p}_A)V_A$ and σ_A are the momentum densities and the anisotropic stress potentials, respectively; with V_x and σ_x being as given by (7) and (9), respectively. The UDE pressure perturbation is given by

$$\delta\rho_x \equiv 2k^2(\alpha_H\mathcal{R} - \alpha_B a^{-2}M^2\mathcal{H}\Pi) + (\alpha_K - 6\alpha_B)\mathcal{H}^2\mathcal{P} - 3\mathcal{H}[(\bar{\rho}_x + \bar{p}_x)\Pi - 2\alpha_B\mathcal{Q}], \quad (\text{A4})$$

and,

$$\begin{aligned} \delta p_x \equiv & \left(\frac{\bar{\rho}_x + \bar{p}_x}{a^{-2}M^2} + 6\alpha_B\mathcal{H}^2 \right) \mathcal{P} - 2\alpha_M\mathcal{H}\mathcal{Q} + \frac{2}{3}k^2\sigma_x \\ & + [\bar{p}'_x + \alpha_M\mathcal{H}a^{-2}M^2(2\mathcal{H}' + \mathcal{H}^2)]\Pi \\ & + 2\alpha_B \left(1 + \frac{\alpha'_B}{\mathcal{H}\alpha_B} + \frac{\mathcal{H}'}{\mathcal{H}^2} + \frac{\mathcal{P}'}{\mathcal{H}\mathcal{P}} \right) \mathcal{H}^2\mathcal{P}, \end{aligned} \quad (\text{A5})$$

where,

$$\mathcal{P} \equiv \frac{M^2}{a^2}(\Pi' + \mathcal{H}\Pi - \Phi), \quad \mathcal{R} \equiv \frac{M^2}{a^2}(\Psi + \mathcal{H}\Pi), \quad (\text{A6})$$

$$\mathcal{Q} \equiv \frac{M^2}{a^2}[\Psi' + \mathcal{H}\Phi + (\mathcal{H}' - \mathcal{H}^2)\Pi]. \quad (\text{A7})$$

For the sake of completeness, we retain in the rest of this appendix the pressure-related parameters for matter.

2. The metric potentials evolution equations

The evolution equations for the metric potentials Π and Ψ are given by

$$\begin{aligned} \Pi' + \left(1 + \frac{\alpha_T - \alpha_M}{\alpha_H} \right) \mathcal{H}\Pi = & \left(\frac{1 + \alpha_H}{\alpha_H} \right) \Phi - \left(\frac{1 + \alpha_T}{\alpha_H} \right) \Psi \\ & + 8\pi G_{\text{eff}} a^2 \frac{\sigma_m}{\alpha_H}, \end{aligned} \quad (\text{A8})$$

where G_{eff} is as given by (1), and

$$\begin{aligned} \Psi' + (1 + \alpha_B)\mathcal{H}\Phi - \alpha_B\mathcal{H}\Pi' + 4\pi G_{\text{eff}} a^2 q_m \\ = \left[\alpha_B - \gamma_{\mathcal{H}} - \frac{4\pi G_{\text{eff}} a^2}{\mathcal{H}^2}(\bar{\rho}_m + \bar{p}_m) \right] \mathcal{H}^2\Pi, \end{aligned} \quad (\text{A9})$$

where $\gamma_{\mathcal{H}} \equiv \mathcal{H}'/\mathcal{H}^2 - 1$, and we have

$$\begin{aligned} \Pi'' + (1 + \gamma_1)\mathcal{H}\Pi' + \gamma_3\mathcal{H}^2\Pi = & \Phi' - \gamma_4\Psi' - \gamma_5\mathcal{H}\Phi \\ & - \gamma_6\mathcal{H}\Psi - \alpha_B \frac{8\pi G_{\text{eff}} a^2}{\gamma_0\mathcal{H}} (2k^2\sigma_m + 3\delta p_m), \end{aligned} \quad (\text{A10})$$

with $\gamma_0 \equiv \alpha_K + 6\alpha_B^2$.

From §II, the parameters γ_1 and γ_3 are given by

$$\begin{aligned} \gamma_1 \equiv & 3 + \alpha_M + \frac{6\alpha_B}{\gamma_0} \left[\frac{\alpha'_B}{\mathcal{H}} - \frac{4\pi G_{\text{eff}} a^2}{\mathcal{H}^2}(\bar{\rho}_m + \bar{p}_m) \right] \\ & + \frac{\alpha'_K}{\mathcal{H}\gamma_0} + (6\alpha_B^2 + 2\alpha_K - 6\alpha_B) \frac{\gamma_{\mathcal{H}}}{\gamma_0}, \end{aligned} \quad (\text{A11})$$

$$\gamma_3 \equiv \gamma_1 + \gamma_2 + \gamma_{\mathcal{H}} + 1, \quad (\text{A12})$$

where $\gamma_{\mathcal{H}}$ is as given by (A9), and

$$\begin{aligned} \gamma_2 \equiv & 6 \left[\frac{\alpha'_B}{\mathcal{H}} + (1 + \alpha_B)\gamma_{\mathcal{H}} + \frac{4\pi G_{\text{eff}} a^2}{\mathcal{H}^2}(\bar{\rho}_m + \bar{p}_m) \right] \frac{\gamma_{\mathcal{H}}}{\gamma_0} \\ & - \frac{2k^2}{\gamma_0\mathcal{H}^2} \left[1 + \alpha_T + \alpha_B(1 + \alpha_B) - (1 + \alpha_H)(1 + \alpha_M) \right. \\ & \quad \left. + \frac{\alpha'_B - \alpha'_H}{\mathcal{H}} + \frac{4\pi G_{\text{eff}} a^2}{\mathcal{H}^2}(\bar{\rho}_m + \bar{p}_m) \right. \\ & \quad \left. + (1 + \alpha_B - \alpha_H)\gamma_{\mathcal{H}} \right] \\ & - 24\pi G_{\text{eff}} a^3 \frac{\alpha_B \bar{p}'_m}{\gamma_0 \mathcal{H}^3}, \end{aligned} \quad (\text{A13})$$

with G_{eff} and $\gamma_{\mathcal{H}}$ being as given by (1) and (A9), respectively, and we have

$$\begin{aligned} \gamma_4 \equiv & 6\gamma_0^{-1} \left[\frac{\alpha'_B}{\mathcal{H}} + (1 + \alpha_B)\gamma_{\mathcal{H}} + \frac{4\pi G_{\text{eff}} a^2}{\mathcal{H}^2}(\bar{\rho}_m + \bar{p}_m) \right] \\ & + \frac{2\alpha_H k^2}{\gamma_0 \mathcal{H}^2}, \end{aligned} \quad (\text{A14})$$

$$\begin{aligned} \gamma_5 \equiv & -(3 + \alpha_M) - \frac{\alpha'_K}{\gamma_0\mathcal{H}} + 6(1 - \alpha_B) \frac{\alpha'_B}{\gamma_0\mathcal{H}} \\ & + \frac{24\pi G_{\text{eff}} a^2}{\gamma_0\mathcal{H}^2}(\bar{\rho}_m + \bar{p}_m)(1 + \alpha_B) \\ & + \left[6 + 12\alpha_B - 6\alpha_B^2 - 2\alpha_K \right] \frac{\gamma_{\mathcal{H}}}{\gamma_0} \\ & + 2(\alpha_H - \alpha_B) \frac{k^2}{\gamma_0\mathcal{H}^2}, \end{aligned} \quad (\text{A15})$$

$$\gamma_6 \equiv \frac{2k^2}{\gamma_0\mathcal{H}^2} \left[\alpha_M + \alpha_H(1 + \alpha_M) - \alpha_T - \frac{\alpha'_H}{\mathcal{H}} \right]. \quad (\text{A16})$$

Note that, except in [2], the parameters $\gamma_1, \gamma_2, \dots, \gamma_6$ are not the same as those in the literature (e.g. [1, 3–7]).

Moreover, by taking the time derivative of (A8), we use (A9) and (A10) to get

$$\begin{aligned} \Phi' + (1 + \lambda_1)\mathcal{H}\Phi = & \lambda_2\mathcal{H}\Psi + \lambda_3\mathcal{H}^2\Pi \\ & + 4\pi G_{\text{eff}} a^2 \left[2\lambda_5\mathcal{H}\sigma_m - \lambda_4q_m - 6\lambda_6 \frac{\delta p_m}{\mathcal{H}} \right], \end{aligned} \quad (\text{A17})$$

where $\lambda_1, \lambda_2, \lambda_3$, and λ_4 are as given in §II, and where $\lambda_1, \lambda_2, \lambda_3$, and λ_4 are as given in §II, and

$$\lambda_5 \equiv \alpha_M + \frac{\alpha'_H}{\mathcal{H}\alpha_H} - \frac{\sigma'_m}{\mathcal{H}\sigma_m} - 2\left(1 + \alpha_H \frac{\alpha_B k^2}{\gamma_0 \mathcal{H}^2}\right) + \frac{\beta_1}{\alpha_H}, \quad (\text{A18})$$

with $\lambda_6 \equiv \alpha_H \alpha_B / \gamma_0$ and, β_1 being as given in §II, and

$$\begin{aligned} \beta_2 \equiv & (\alpha_M - \alpha_T) \frac{\alpha'_H}{\alpha_H \mathcal{H}} + (\alpha_H - \alpha_M + \alpha_H \gamma_4 - 1) \frac{\mathcal{H}'}{\mathcal{H}^2} \\ & + \lambda_4 \left[1 + \alpha_B - \frac{4\pi G_{\text{eff}} a^2}{\mathcal{H}^2} (\bar{\rho}_m + \bar{p}_m) \right] \\ & + \frac{\alpha'_T - \alpha'_M}{\mathcal{H}} - \alpha_H \gamma_3. \end{aligned} \quad (\text{A19})$$

Appendix B: The Energy-momentum Tensor

We use the energy-momentum tensor for fluids:

$$T^0_0 = -(\bar{\rho} + \delta\rho), \quad (\text{B1})$$

$$T^0_j = (\bar{\rho} + \bar{p}) \nabla_j V, \quad (\text{B2})$$

$$T^i_j = (\bar{p} + \delta p) \delta^i_j + \left(\nabla^i \nabla_j - \frac{1}{3} \delta^i_j \nabla^2 \right) \sigma, \quad (\text{B3})$$

where $\bar{\rho}$ and \bar{p} are the background energy density and pressure, respectively; with $\delta\rho$ and δp being the perturbed energy density and pressure, respectively; σ is the anisotropic stress potential, V being the (gauge-invariant) velocity potential.

-
- [1] J. Gleyzes, D. Langlois, and F. Vernizzi, A unifying description of dark energy, *Int. J. Mod. Phys. D* **23**, 1443010 (2015), arXiv:1411.3712 [hep-th].
- [2] D. Duniya, T. Moloi, C. Clarkson, J. Larena, R. Maartens, B. Mongwane, and A. Weltman, Probing beyond-Horndeski gravity on ultra-large scales, *JCAP* **01**, 033, arXiv:1902.09919 [astro-ph.CO].
- [3] L. Lombriser and A. Taylor, Semi-dynamical perturbations of unified dark energy, *JCAP* **11**, 040, arXiv:1505.05915 [astro-ph.CO].
- [4] J. Sakstein, H. Wilcox, D. Bacon, K. Koyama, and R. C. Nichol, Testing Gravity Using Galaxy Clusters: New Constraints on Beyond Horndeski Theories, *JCAP* **07**, 019, arXiv:1603.06368 [astro-ph.CO].
- [5] J. Gleyzes, D. Langlois, F. Piazza, and F. Vernizzi, Exploring gravitational theories beyond Horndeski, *JCAP* **02**, 018, arXiv:1408.1952 [astro-ph.CO].
- [6] J. Gleyzes, D. Langlois, F. Piazza, and F. Vernizzi, Healthy theories beyond Horndeski, *Phys. Rev. Lett.* **114**, 211101 (2015), arXiv:1404.6495 [hep-th].
- [7] E. Bellini and I. Sawicki, Maximal freedom at minimum cost: linear large-scale structure in general modifications of gravity, *JCAP* **07**, 050, arXiv:1404.3713 [astro-ph.CO].
- [8] I. D. Saltas and I. Lopes, Obtaining Precision Constraints on Modified Gravity with Helioseismology, *Phys. Rev. Lett.* **123**, 091103 (2019), arXiv:1909.02552 [astro-ph.CO].
- [9] I. D. Saltas and J. Christensen-Dalsgaard, Searching for dark energy with the Sun, *Astron. Astrophys.* **667**, A115 (2022), arXiv:2205.14134 [astro-ph.SR].
- [10] T. Clifton, P. G. Ferreira, A. Padilla, and C. Skordis, Modified Gravity and Cosmology, *Phys. Rept.* **513**, 1 (2012), arXiv:1106.2476 [astro-ph.CO].
- [11] M. Ishak, Testing General Relativity in Cosmology, *Living Rev. Rel.* **22**, 1 (2019), arXiv:1806.10122 [astro-ph.CO].
- [12] K. Bamba, S. Capozziello, S. Nojiri, and S. D. Odintsov, Dark energy cosmology: the equivalent description via different theoretical models and cosmography tests, *Astrophys. Space Sci.* **342**, 155 (2012), arXiv:1205.3421 [gr-qc].
- [13] D. Duniya, Large-scale imprint of relativistic effects in the cosmic magnification, *Phys. Rev. D* **93**, 103538 (2016), [Addendum: *Phys. Rev. D* **93**, 129902 (2016)], arXiv:1604.03934 [astro-ph.CO].
- [14] D. Duniya, D. Bertacca, and R. Maartens, Clustering of quintessence on horizon scales and its imprint on HI intensity mapping, *JCAP* **10**, 015, arXiv:1305.4509 [astro-ph.CO].
- [15] D. Duniya, D. Bertacca, and R. Maartens, Probing the imprint of interacting dark energy on very large scales, *Phys. Rev. D* **91**, 063530 (2015), arXiv:1502.06424 [astro-ph.CO].
- [16] D. Duniya, Dark energy homogeneity in general relativity: Are we applying it correctly?, *Gen. Rel. Grav.* **48**, 52 (2016), arXiv:1505.03436 [gr-qc].
- [17] E. J. Copeland, M. Sami, and S. Tsujikawa, Dynamics of dark energy, *Int. J. Mod. Phys. D* **15**, 1753 (2006), arXiv:hep-th/0603057.
- [18] M. Bartelmann and P. Schneider, Weak gravitational lensing, *Phys. Rept.* **340**, 291 (2001), arXiv:astro-ph/9912508.
- [19] C. Bonvin, Effect of Peculiar Motion in Weak Lensing, *Phys. Rev. D* **78**, 123530 (2008), arXiv:0810.0180 [astro-ph].
- [20] B. Gillis and A. Taylor, A Generalized Method for Measuring Weak Lensing Magnification With Weighted Number Counts, *Mon. Not. Roy. Astron. Soc.* **456**, 2518 (2016), arXiv:1507.01858 [astro-ph.CO].
- [21] K. Umetsu, A. Zitrin, D. Gruen, J. Merten, M. Donahue, and M. Postman, CLASH: Joint Analysis of Strong-Lensing, Weak-Lensing Shear and Magnification Data for 20 Galaxy Clusters, *Astrophys. J.* **821**, 116 (2016), arXiv:1507.04385 [astro-ph.CO].
- [22] D. Jeong, F. Schmidt, and C. M. Hirata, Large-scale clustering of galaxies in general relativity, *Phys. Rev. D* **85**, 023504 (2012), arXiv:1107.5427 [astro-ph.CO].
- [23] D. J. Bacon, S. Andrianomena, C. Clarkson, K. Bolejko, and R. Maartens, Cosmology with Doppler Lensing, *Mon. Not. Roy. Astron. Soc.* **443**, 1900 (2014), arXiv:1401.3694 [astro-ph.CO].
- [24] A. Raccanelli, D. Bertacca, D. Jeong, M. C. Neyrinck, and A. S. Szalay, Doppler term in the galaxy two-point correlation function: wide-angle, velocity, Doppler lensing and cosmic acceleration effects, *Phys. Dark Univ.* **19**, 109 (2018), arXiv:1602.03186 [astro-ph.CO].

- [25] S. Andrianomena, C. Bonvin, D. Bacon, P. Bull, C. Clarkson, R. Maartens, and T. Moloi, Testing General Relativity with the Doppler magnification effect, *Mon. Not. Roy. Astron. Soc.* **488**, 3759 (2019), arXiv:1810.12793 [astro-ph.CO].
- [26] D. Duniya, A. Abebe, A. de la Cruz-Dombriz, and P. K. S. Dunsby, Imprint of $f(R)$ gravity in the cosmic magnification, *Mon. Not. Roy. Astron. Soc.* **518**, 6102 (2022), arXiv:2210.09303 [astro-ph.CO].
- [27] D. Duniya and M. Kumwenda, Which is a better cosmological probe: number counts or cosmic magnification?, *Mon. Not. Roy. Astron. Soc.* **522**, 3308 (2023), arXiv:2203.11159 [astro-ph.CO].
- [28] D. H. Weinberg, M. J. Mortonson, D. J. Eisenstein, C. Hirata, A. G. Riess, and E. Rozo, Observational Probes of Cosmic Acceleration, *Phys. Rept.* **530**, 87 (2013), arXiv:1201.2434 [astro-ph.CO].
- [29] L. Van Waerbeke, Shear and Magnification: Cosmic Complementarity, *Mon. Not. Roy. Astron. Soc.* **401**, 2093 (2010), arXiv:0906.1583 [astro-ph.CO].
- [30] C. Duncan, B. Joachimi, A. Heavens, C. Heymans, and H. Hildebrandt, On the complementarity of galaxy clustering with cosmic shear and flux magnification, *Mon. Not. Roy. Astron. Soc.* **437**, 2471 (2014), arXiv:1306.6870 [astro-ph.CO].
- [31] C. Bonvin and R. Durrer, What galaxy surveys really measure, *Phys. Rev. D* **84**, 063505 (2011), arXiv:1105.5280 [astro-ph.CO].
- [32] D. Duniya, Understanding the relativistic overdensity of galaxy surveys, arXiv:1606.00712 (2016), arXiv:1606.00712 [astro-ph.CO].
- [33] J. B. Dent and S. Dutta, On the dangers of using the growth equation on large scales, *Phys. Rev. D* **79**, 063516 (2009), arXiv:0808.2689 [astro-ph].
- [34] I. Harry and J. Noller, Probing the speed of gravity with LVK, LISA, and joint observations, *Gen. Rel. Grav.* **54**, 133 (2022), arXiv:2207.10096 [gr-qc].
- [35] J. Noller and A. Nicola, Cosmological parameter constraints for Horndeski scalar-tensor gravity, *Phys. Rev. D* **99**, 103502 (2019), arXiv:1811.12928 [astro-ph.CO].
- [36] A. W. Blain, Exploiting magnification bias in ultradeep submillimetre-wave surveys using alma, *Mon. Not. Roy. Astron. Soc.* **330**, 219 (2002), arXiv:astro-ph/0110403.
- [37] R. Ziour and L. Hui, Magnification Bias Corrections to Galaxy-Lensing Cross-Correlations, *Phys. Rev. D* **78**, 123517 (2008), arXiv:0809.3101 [astro-ph].
- [38] F. Schmidt, E. Rozo, S. Dodelson, L. Hui, and E. Sheldon, Size Bias in Galaxy Surveys, *Phys. Rev. Lett.* **103**, 051301 (2009), arXiv:0904.4702 [astro-ph.CO].
- [39] S. Camera, C. Fedeli, and L. Moscardini, Magnification bias as a novel probe for primordial magnetic fields, *JCAP* **03**, 027, arXiv:1311.6383 [astro-ph.CO].
- [40] H. Hildebrandt, Observational biases in flux magnification measurements, *Mon. Not. Roy. Astron. Soc.* **455**, 3943 (2016), arXiv:1511.01352 [astro-ph.GA].
- [41] S. Dodelson, *Modern Cosmology* (Academic Press, 2003).
- [42] P. A. R. Ade *et al.* (Planck), Planck 2015 results. XIII. Cosmological parameters, *Astron. Astrophys.* **594**, A13 (2016), arXiv:1502.01589 [astro-ph.CO].
- [43] D. Alonso and P. G. Ferreira, Constraining ultralarge-scale cosmology with multiple tracers in optical and radio surveys, *Phys. Rev. D* **92**, 063525 (2015), arXiv:1507.03550 [astro-ph.CO].
- [44] J. Fonseca, S. Camera, M. Santos, and R. Maartens, Hunting down horizon-scale effects with multi-wavelength surveys, *Astrophys. J. Lett.* **812**, L22 (2015), arXiv:1507.04605 [astro-ph.CO].
- [45] A. Witzemann, D. Alonso, J. Fonseca, and M. G. Santos, Simulated multitracer analyses with H I intensity mapping, *Mon. Not. Roy. Astron. Soc.* **485**, 5519 (2019), arXiv:1808.03093 [astro-ph.CO].
- [46] P. Paul, C. Clarkson, and R. Maartens, Wide-angle effects in multi-tracer power spectra with Doppler corrections, *JCAP* **04**, 067, arXiv:2208.04819 [astro-ph.CO].
- [47] D. Karagiannis, R. Maartens, J. Fonseca, S. Camera, and C. Clarkson, Multi-tracer power spectra and bispectra: Formalism, arXiv:2305.04028 (2023), arXiv:2305.04028 [astro-ph.CO].
- [48] R. Zhao *et al.*, A Multi-tracer Analysis for the eBOSS galaxy sample based on the Effective Field Theory of Large-scale Structure, arXiv:2308.06206 (2023), arXiv:2308.06206 [astro-ph.CO].
- [49] P. R. Bevington and D. K. Robinson, *Data Reduction and Error Analysis for Physical Sciences*, 3rd ed. (McGraw-Hill, 2003).
- [50] Wikipedia, Propagation of uncertainty, https://en.wikipedia.org/wiki/Propagation_of_uncertainty.
- [51] K. S. Dawson *et al.* (BOSS), The Baryon Oscillation Spectroscopic Survey of SDSS-III, *Astron. J.* **145**, 10 (2013), arXiv:1208.0022 [astro-ph.CO].
- [52] R. Maartens, F. B. Abdalla, M. Jarvis, and M. G. Santos (SKA Cosmology SWG), Overview of Cosmology with the SKA, *PoS AASKA14*, 016 (2015), arXiv:1501.04076 [astro-ph.CO].